Cell-type specific contributions to theta-gamma coupled rhythms in the hippocampus

Spandan Sengupta[1†], **Afroditi Talidou**[1,2†], **Jeremie Lefebvre**[1,2,3‡], **Frances K Skinner**[1,4‡*]

***For correspondence:** frances.skinner@uhn.ca (FKS)

[†]These authors contributed equally to this work
[‡]These senior authors contributed equally to this work

[1]Krembil Brain Institute, University Health Network; [2]Department of Biology, University of Ottawa; [3]Department of Mathematics, University of Toronto; [4]Department of Physiology, University of Toronto

Abstract

The distinct inhibitory cell types that participate in cognitively relevant nested brain rhythms require that model circuits reflect this diversity. The co-expression of theta and gamma rhythms may represent a general coding scheme and particular changes in these coupled rhythms occur in disease states. We develop a population rate model of the CA1 hippocampus that encompasses circuits of three inhibitory cell types (bistratified cells, parvalbumin (PV)-expressing and cholecystokinin (CCK)-expressing basket cells) and pyramidal cells to examine coupled rhythms. We constrain parameters and perform theoretical and numerical analyses of the model. We find that CCK-expressing basket cells initiate the coupled rhythms and regularize theta, and PV-expressing basket cells enhance both theta and gamma rhythms. Pyramidal and bistratified cells govern the generation of theta rhythms, PV-expressing basket and pyramidal cells play dominant roles in controlling theta frequencies. We predict circuit motifs for theta-gamma coupled rhythms which may be generally applicable.

Introduction

Oscillatory activities of wide-ranging frequencies are ubiquitous in many brain structures (***Buzsáki, 2006***). In particular, the hippocampus expresses such well-defined rhythmic activities with functional and behavioural correlates (***Colgin, 2016***). Theta oscillations, ranging from 3 to 12 Hz, are prominent local field potential (LFP) rhythms that are most robustly recorded from the CA1 region (***Buzsáki, 2002***). This rhythm plays an essential role in memory and spatial navigation (***Buzsáki and Moser, 2013***), with its frequency being related to the animal's kinematics (***Kropff et al., 2021***). High (7-12 Hz) and low (4-7 Hz) ranges of theta frequencies dependent on atropine sensitivity have long been observed (***Buzsáki, 2002***; ***Kramis et al., 1975***), and these high or low frequencies can be distinctly elicited by social or fearful stimuli, respectively (***Tendler and Wagner, 2015***). A single theta cycle has been considered to be 'a functional unit capable of representing distinct temporal-spatial content at different phases' (***Wilson et al., 2015***), and higher frequency gamma (≈20-100 Hz) oscillations are nested within these theta cycles (e.g., see ***Scheffer-Teixeira et al.*** (***2012***)). It has been suggested that such theta-gamma coupling is a general coding scheme with information processing implications (***Jensen and Colgin, 2007***; ***Lisman, 2005***; ***Colgin, 2015***). Dynamic modulation of theta-gamma coupled rhythms during sleep (***Bandarabadi et al., 2019***), visual exploration (***Kragel et al., 2020***) and association with working memory exists, and it is thus not surprising that there is

increasing evidence of specific changes in theta-gamma coupling with memory impairments, disease and its progression (***Goutagny et al., 2013***; ***Hamm et al., 2015***; ***Karlsson et al., 2022***; ***Kitchigina, 2018***; ***Musaeus et al., 2020***; ***Zhang et al., 2016***). Yet, it remains unclear what cell circuit motifs and mechanism(s) responsible for their generation and co-expression are involved. Identifying the features involved — ranging from cell types to the way they connect to each other — represents a formidable interdisciplinary challenge with important biomedical relevance.

It is clear that the hippocampus is characterized by many diverse sets of interneuron or inhibitory cell types (***Freund and Buzsáki, 1996***; ***Kessaris and Denaxa, 2023***). It is important to consider this diversity as functionally relevant rhythmic activities (i.e., theta and gamma) arise from dynamic interactions of these various inhibitory and excitatory cell types in brain circuits (***Buzsáki, 2006***; ***Fishell and Kepecs, 2020***; ***Kepecs and Fishell, 2014***; ***Klausberger and Somogyi, 2008***; ***McBain and Fisahn, 2001***). For example, in trying to understand the contributions of specific inhibitory cell types, it has long been noted that there is a separation between perisomatically and dendritically targeting interneuron types onto pyramidal cells (***Freund and Buzsáki, 1996***; ***McBain and Fisahn, 2001***) leading to consideration of a dichotomy in inhibitory control of pyramidal cell excitability. Further, ***Freund*** (***2003***) has described another dichotomy of perisomatically targeting cholecystokinin (CCK)-expressing and parvalbumin (PV)-expressing basket cells in a 'rhythm and mood' fashion (***Freund, 2003***; ***Freund and Katona, 2007***) – PV-expressing basket cells contribute in a precise clockwork fashion, and CCK-expressing basket cells in a highly modulatory way. Today, new technologies are leading to clear delineations of distinct inhibitory cell types (***Kessaris and Denaxa, 2023***; ***Ratliff and Batista-Brito, 2020***) which will help bridge cell-type focused experimental and mathematical modeling studies.

Many mathematical circuit models have been developed to help decipher the complicated excitatory and inhibitory interactions underlying theta-gamma coupled rhythms in the hippocampus (***Ferguson and Skinner, 2015***). Several developed circuit models have included explicitly identified and characterized cell types (***Bezaire et al., 2016***; ***Ferguson et al., 2017***; ***Ecker et al., 2020***). However, the nonlinear, high dimensional and dynamic nature of such systems challenges our capacity to extract explicit mechanisms. To circumvent this limitation, we here build and analyze a cell-type specific mean field model that combines pyramidal cells and three distinct inhibitory cell types (bistratified cells, PV-expressing and CCK-expressing basket cells), that were found to be essential for theta-gamma coupled rhythms from cell-type and cell-type interaction perspectives (***Bezaire et al., 2016***; ***Chatzikalymniou et al., 2022***). This model leverages population-scale description of neural activity with experimentally constrained parameters to gather insight about theta-gamma coupling and theta frequency control in the hippocampus, while providing testable predictions.

We perform high-throughput simulations to fit and constrain our model parameters. We systematically analyze the contribution of individual cell types and connectivity motifs involved in theta-gamma coupled oscillations by quantifying changes in spectral characteristics resulting from targeted stimulation of individual cell types. We perform theoretical analysis which, in combination with numerical explorations, predicts cell types and motifs essential for co-existence of theta and gamma oscillations. We examine whether particular cell types play dominant roles in the control of theta frequency. We find a plethora of datasets that allow the expression of theta-gamma coupled rhythms, indicating degeneracy underlying theta-gamma coupling. We find that circuit motifs of pyramidal and bistratified cells play a governing role in the theta rhythms, with CCK-expressing and PV-expressing basket cells together with pyramidal cells contributing to gamma rhythms. We discover that CCK-expressing basket cells act to initiate theta-gamma coupled rhythms by their ability to control pyramidal cell activity via disinhibition, and we present a general two-phase process by which theta-gamma coupled rhythms arise in four-cell network motifs of inhibitory and excitatory cells.

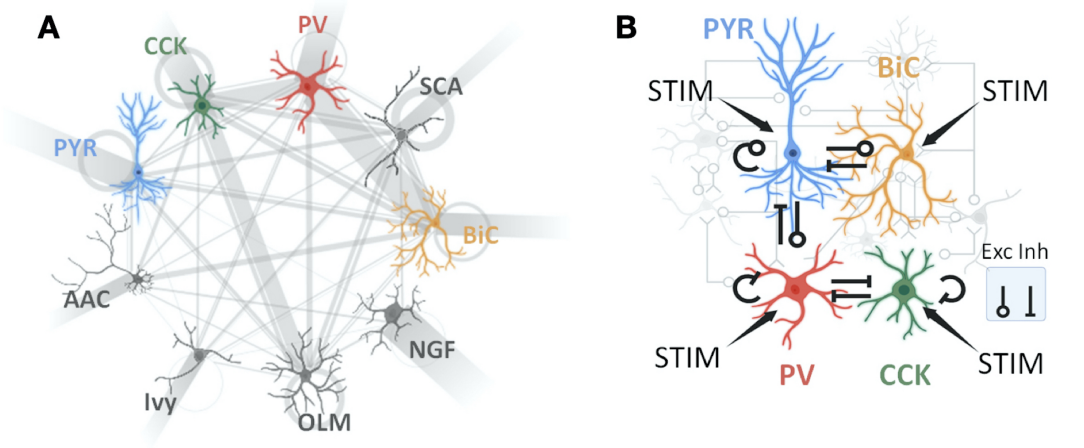

Figure 1. Schematics of microcircuit models of CA1 hippocampus.
A. Stylized schematic showing the nine different cell types that are present in a detailed circuit model of CA1 hippocampus (***Bezaire et al., 2016***). These cell types are pyramidal cells, paravalbumin-expressing basket cells, axo-axonic cells, bistratified cells, cholecystokinin-expressing basket cells, Schaeffer Collateral-associated cells, oriens-lacunosum-moleculare cells, neurogliaform cells, and Ivy cells. They are referred to as PYR, PV, AAC, BiC, CCK, SCA, OLM, NGF, Ivy, respectively. Connections between the different cell types are represented by grey lines between them. Grey circles by a given cell type indicate that they are interconnected, and incoming grey lines to the different cell types represent external drives. The thickness of the lines and circles is representative of the relative strength of these various connections. **B.** Stylized schematic of the reduced model with four cell types (PYR, BiC, CCK, PV) and excitatory (Exc) and inhibitory (Inh) connections between them with possible inputs (STIM) to each cell type. The rationale used to consider this reduced model is given in the main text.

Results

In order to disambiguate the respective role of cell types and their mutual connectivity motifs in the generation and control of theta-gamma coupled rhythms in the CA1 hippocampus, we developed a reduced, system-level mean field population rate model (PRM). This model combines connections and cell types that were identified as critical for the existence of theta-gamma rhythms based on previous work using more detailed circuit models with nine different cell types (pyramidal cells, bistratified cells, PV-expressing basket cells, CCK-expressing basket cells, axo-axonic cells, Schaeffer collateral-associated cells, ivy cells, neurogliaform cells and oriens-lacunosum-moleculare cells) (***Bezaire et al., 2016***; ***Chatzikalymniou et al., 2021***, ***2022***). Specifically, we have previously shown that the initiation of theta rhythms requires the presence of excitatory coupling between pyramidal cells (***Chatzikalymniou et al., 2021***), and that theta rhythms are lost with the removal of certain connections (***Chatzikalymniou et al., 2022***). In summary, we rationalize the use of a four cell-type microcircuit based on the more elaborate nine cell-type microcircuit (***Bezaire et al., 2016***; ***Chatzikalymniou et al., 2022***) to examine theta-gamma coupled rhythms in CA1 hippocampus. The four cell types are pyramidal cells, bistratified cells and PV-expressing and CCK-expressing basket cells. Moving forward, we will refer to pyramidal cells as **PYR**, bistratified cells as **BiC**, CCK-expressing basket cells as **CCK**, and PV-expressing basket cells as **PV**. In FIGURE 1, we show schematics of the cell types and interconnections used in previous detailed microcircuit models of the CA1 hippocampus (**A**), and the four cell-type microcircuit used here (**B**).

A population rate model (PRM) of theta-gamma coupled rhythms

We build a PRM of the four cell microcircuit depicted in FIGURE 1B, and explore it using a combination of techniques. Mathematical equations and parameter descriptions are provided in the Model and methods section. This PRM is novel relative to other mean field models in its incorporation of distinct cell types, particular interconnectivities and dynamics that speak of both theta and

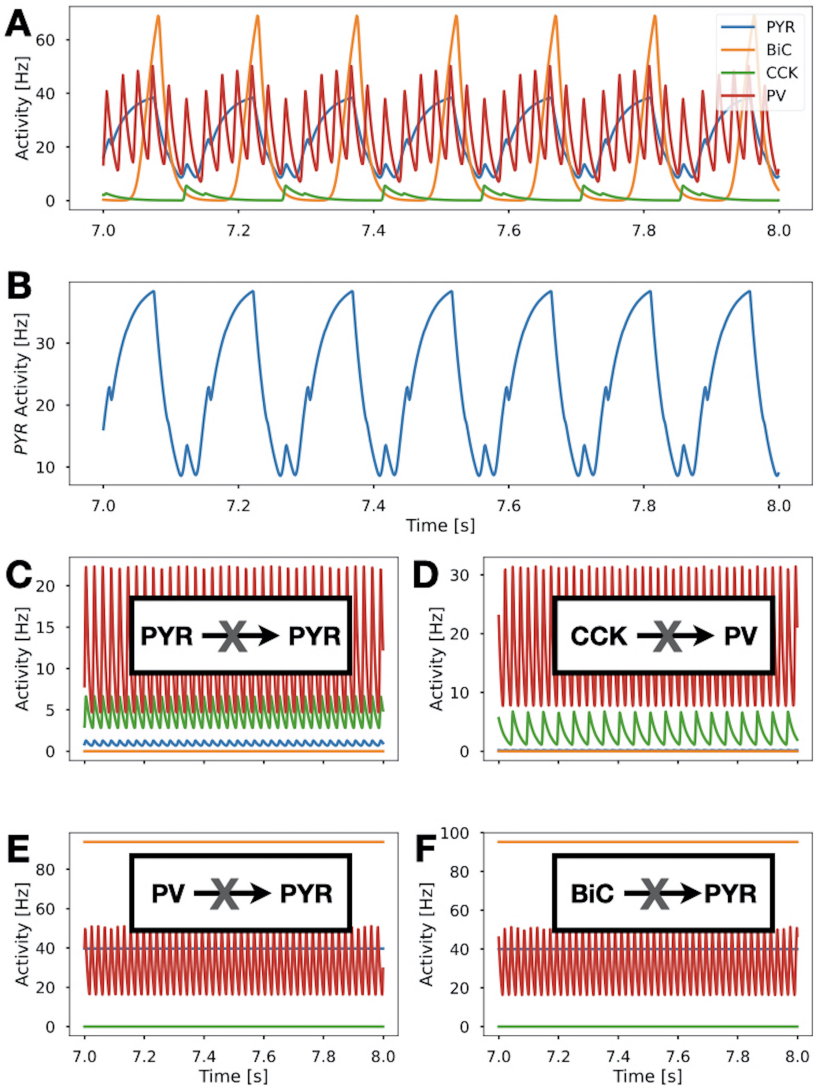

Figure 2. An example of PRM output.
A. Activity of the four cell types (PYR, BiC, CCK, PV) in the PRM at baseline (i.e., when no STIM is applied to any of the cell types) over a one second interval. Colors match those shown in the schematic of FIGURE 1B of the four cell-type circuit. The synaptic weight parameter values used in this simulation are from *Set 4* in TABLE 2. **B.** Activity of only PYR showing theta-gamma coupled rhythms. PYR output is analyzed as an LFP representation. **C-F.** Removal of connections between cell types as schematized in each panel. These connections were previously shown to be required for theta-gamma coupled rhythms. See text for further detail.

Figure 2—figure supplement 1. Intrinsic firing rates for the four cell-types in the PRM.

gamma oscillations and their co-existence. Its deliberate simplicity, compared to other detailed computational models developed previously (e.g., ***Bezaire et al.*** (***2016***)), represents an important advantage as it enables a thorough exploration of parameter space with constrained values and a detailed mathematical characterization of different cell-type contributions. Since extracellular LFP recordings are typically done in the pyramidal cell layer with PYR constituting the vast majority of the cells in the network, we consider PYR activity as representing the LFP output. The PRM exhibits LFP oscillations within gamma and theta frequency bands that are coupled with one another. An example is shown in FIGURE 2**A**. We show the activities of all four cell types (PYR, BiC, CCK, PV) in FIGURE 2**A**, and only PYR in FIGURE 2**B** to more easily visualize the LFP representation of theta-gamma coupled rhythms.

To better understand theta-gamma coupled rhythms, we first obtained constrained parameter sets which revealed degeneracy and variability of the different connection types. We then performed theoretical analyses on subsystems of the PRM which produced cellular insights into theta and gamma rhythm generation. Subsequently, we carried out extensive numerical simulations to expose contributions by the different cell types. Finally, using our combined theoretical and numerical insights, we present cell-type specific roles and motifs underlying the expression of theta-gamma coupled rhythms.

Degeneracy and variability in the PRM

The co-existence of theta and gamma oscillations, as illustrated in FIGURE 2**B**, results from a combination of excitation-inhibition motifs, and delayed feedback. The frequency and power of these theta-gamma coupled rhythms are controlled by a combination of parameters. To determine which parameter combinations allow theta-gamma coupled rhythms in the PRM, we first applied constraints from the experimental literature for each of the four different cell types, while setting parameters to values that produce coupled oscillations within rationalized constraints (see Model and methods section). In doing this, we ensured that the overall dynamics of the network and relative differences in cell type properties were both taken into consideration.

One such important constraint is the manifest loss of theta activity following connection removal. Based on previous simulation studies using detailed network models (***Chatzikalymniou et al., 2021***, ***2022***), theta oscillations should no longer be present whenever connections between PYR and PYR, from CCK to PV, from PV to PYR, and from BiC to PYR, are removed. This constraint guided our parameter search: from an initial set of parameter values, we used a genetic algorithm search in the parameter space of the synaptic weights (w) and obtained 200 sets of synaptic weights satisfying the above criterion. For the example parameter set of FIGURE 2, we show in **C-F** that the constraint of connection removals is satisfied.

The multiple sets of w obtained illustrate the degeneracy of the model system producing theta-gamma coupled rhythms. The distribution of these 200 sets of w is shown in FIGURE 3**A**. The variability differs for the nine different connection types, and this can be appreciated by observing their standard deviations (std) shown in the bar graph histogram of FIGURE 3**B**. Noting the large std for the synaptic weights involving CCK, we re-ran the genetic algorithm with an adjusted constraint regarding CCK. The outcome is shown in the *Supplementary Figure* of FIGURE 3. As expected, we obtained changes for the different synaptic weights, but the relative sizes of the synaptic weights remained the same, and the CCK→PV connection remained as a synaptic weight with one of the largest std. The PYR→PYR connection had the largest synaptic weight for excitatory connections, and for inhibitory connections, the largest synaptic weights involved CCK: CCK→CCK and CCK→PV. Overall, these results suggest that CCK may have a specific role relative to the other cell types.

From the 200 parameter sets shown in FIGURE 3**A**, we applied clustering techniques and selected ten parameter sets (see Model and methods section for details) for further analyses. These ten chosen parameter sets (*Sets 0-9*) represent a spectrum of synaptic weight parameter values that generate theta-gamma coupled rhythms in the PRM. Values of the synaptic weights for each of the nine different connections is given in columns 2-5 of TABLE 2. Columns 6 and 7 provide the ratio of PV and BiC activities and the maximal CCK activity for each of the ten sets - these characteristics were used as part of the constraints when the genetic algorithm was applied (see Model and methods section).

To start to derive an understanding of the contributions of the different connections between the different cell types, we examined LFPs (i.e., PYR activity outputs) when each of the nine different connection types were removed, using the ten parameter sets (TABLE 2). We show the results of this in TABLE 3, where the change in theta or gamma power is shown, as well as whether theta-gamma coupled rhythms are present when a particular connection is removed. First, as it was part of the constraints, theta rhythms were not present in any of the ten sets when PYR→PYR or CCK→PV

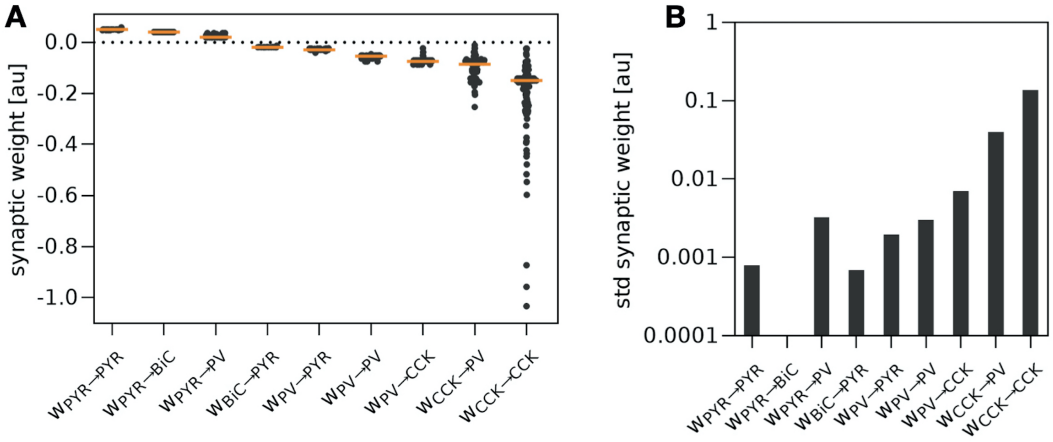

Figure 3. Distributions of constrained synaptic weights.
A. Distribution of synaptic weights for each of the nine different connections in the PRM, from the 200 constrained parameter sets of synaptic weights found using a genetic algorithm. The orange line depicts the median. **B.** Bar graph showing the standard deviations (std) of the synaptic weights for each of the nine different connections.

Figure 3—figure supplement 1. Additional distributions.

or PV→PYR or BiC→PYR connections were removed. Gamma rhythms remained when PYR→PYR or CCK→PV were removed, but not when the other two connection types were removed. For three of the other five connection types, PV→CCK or PYR→PV or CCK→CCK, it was possible to have theta-gamma coupled rhythms when they were removed. This is detailed in TABLE 3. Thus, these results are also suggestive of CCK having a more particular role in the four-cell circuit generating theta-gamma coupled rhythms. Using these ten parameter sets, we now move to theoretical analysis considerations.

Theoretical analyses predict circuit motifs underlying theta and gamma rhythms

To gain insights into the cell types and connectivity motifs contributing to the generation and interaction of theta and gamma rhythms, we leveraged linear stability analysis. Capitalizing on the parameter sets we identified above, we systematically examined the connectivity motifs responsible for generating oscillations in both the theta and gamma frequency bands. To achieve this, we dissected the PRM (see Eqs. (1a)-(1d) in Model and methods section) into three distinct and independent motifs — specifically PYR and BiC (PYR+BiC), PYR and PV (PYR+PV) and CCK and PV (CCK+PV) — each corresponding to a subsystem of dimension two. This approach enabled us to examine the behaviour of each motif, thereby enhancing our understanding of their contributions to theta and/or gamma activity. Additional details can be found in the Model and methods section.

While many parameters could have been considered, we focused our analysis on the role of delays due to their well-known influence on oscillatory behaviour. We found that these delays play a crucial role in enabling the co-existence of oscillations with different frequencies. Our analysis revealed that the dynamics of PYR+BiC are instrumental in generating rhythms within the theta band, whereas both PYR+PV and CCK+PV motifs independently generate gamma frequency rhythms.

Limit cycles form around the equilibrium points demonstrating the activity of the cell types. Trajectory activities for the various subsystems are plotted for different delay values in FIGURE 4: PYR+BiC in (**A**), PYR+PV in (**B**), and CCK+PV in (**C**). Activities of the cell types for the three subsystems as a function of time using a five millisecond time delay are shown in FIGURE 4**D, E, F.** In a summary plot (FIGURE 4**G**), the frequencies of the three subsystems are depicted as a function of delays. For each subsystem, we plotted the activity of only one cell type because either the second cell type remains silent or exhibits a very small amplitude, as indicated by the limit cycles. Notably,

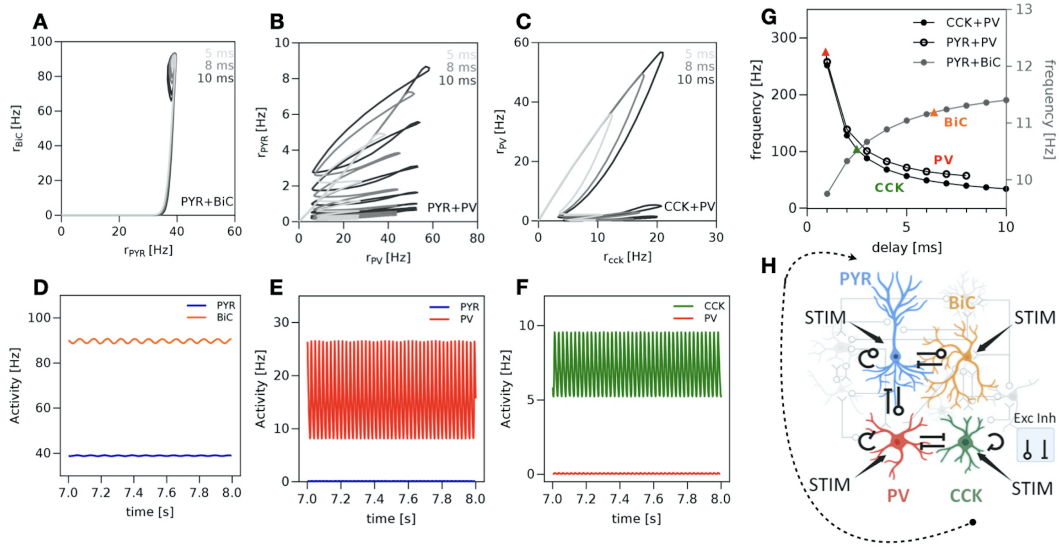

Figure 4. Theoretical analyses of PRM subsystems.
Limit cycles around equilibrium points for the PYR+BiC (**A**), PYR+PV (**B**) and CCK+PV (**C**) subsystems. **D.** Activity of the two cell types (PYR, BiC) in PYR+BiC subsystem over a one second interval showing theta rhythms. **E.** Activity of the two cell types (PYR, PV) in PYR+PV subsystem. PYR is silent while PV exhibit gamma frequencies. **F.** Activity of CCK and PV in the CCK+PV subsystem. The CCK oscillate with gamma frequencies while PV demonstrate only a small amplitude and activity. Delays in **D**, **E** and **F** have been fixed to 5 ms. **G.** Frequencies plotted for BiC, PV and CCK as a function of different delay values. The coloured triangles show the bifurcation points (that is, delays) for the three subsystems (PYR+BiC, PYR+PV and CCK+PV). **H.** Schematic illustration of the inhibition mechanism of PYR initiated by CCK. *Set 0* parameter values were used in the calculations for these plots.

the frequency of PYR+BiC consistently remains in the theta band across all selected delay values. In contrast, CCK+PV and PYR+PV subsystems demonstrate higher frequencies than gamma for small delays. Nevertheless, as delays increase, the associated frequency values decrease, ultimately settling within the gamma band. Hopf bifurcations arise at different delays. To maintain simplicity in our model, for the remainder of the study, we fix the delay at a value at which our analysis predicts the co-existence of both theta and gamma frequencies. We choose five milliseconds considering physiological axon conduction delays and synaptic activation time values (***Traub et al., 1992***).

The activation of CCK in the CCK+PV subsystem (FIGURE 4**F**) and PV in the PYR+PV subsystem (FIGURE 4**E**) suggest a potential relationship between the initiation of gamma frequencies and the inhibition of PYR through a mechanism where CCK is implicated in the initiation of gamma frequencies and PV subsequently when it inhibits PYR cells. This suggestion is schematized in FIGURE 4**H**. The parameter values used in FIGURE 4 are from *Set 0*. However, the general result holds for all of the ten parameter sets (see parameter values in TABLE 2).

Numerical explorations

We systematically explored our four-cell circuit by applying a STIM input to each of the four different cell types (see FIGURE 1**B**), using the ten different parameter sets (TABLE 2). We performed simulations for a wide range of STIM values and measured stimulation ranges over which theta-gamma coupled rhythms persist to assess the robustness of the coupling and the roles played by the different cell types in influencing their existence. To do this, we extracted theta and gamma powers as well as theta frequencies from the theta-gamma coupled rhythms.

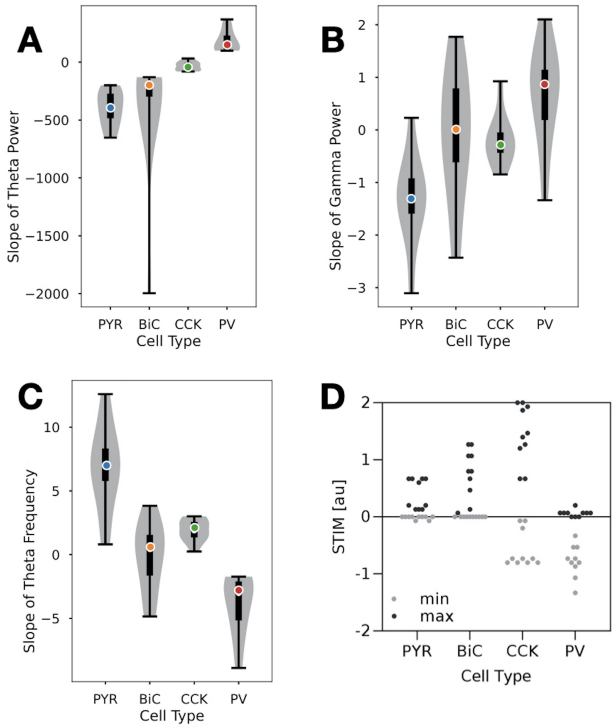

Figure 5. Cell type sensitivities.
STIM values are applied to each cell type for each of the ten parameter sets (TABLE 2). Theta and gamma powers and theta frequency are extracted when theta-gamma coupled rhythms are present. Violin plots show the distribution of the slope of the theta power (**A**), gamma power (**B**) and theta frequency (**C**) with increasing STIM to each cell type. The slope is derived from a linear best-fit (see *Supplementary Figure*) through the points where the system exhibits theta-gamma coupled rhythms (see Model and methods section for further details). For all of the plots in *A-C*, the thick bar extends from the first quartile (Q1) to the third quartile (Q3) of the data, with the circle at the median. The color of the circles is representative of the cell type (see FIGURE 1B). The whiskers capture the full range of the data and the translucent 'violin' captures the smoothed probability distribution of the data. **D.** Minimum (min) and maximum (max) STIM values to the different cell types that allowed theta-gamma coupled rhythms to be expressed.

Figure 5—figure supplement 1. Example illustration of slope quantification for theta and gamma powers and theta frequency with STIM variation.

Figure 5—figure supplement 2. Example illustration of PYR activities and their power spectral densities.

Numerics support theoretical predictions for circuit motifs underlying theta and gamma rhythm generation

The theory predicted that PYR+BiC circuits can function as theta frequency rhythm generators, but not any of the other two cell subsystems. For gamma rhythms, the theory indicated that either PYR+PV or CCK+PV (or both) lead to gamma frequency rhythm expression. To consider this in the full four-cell circuit, we examined STIM values which preserved the theta-gamma regime and determined how sensitive the spectral properties of the co-existing oscillations were to selective stimulation. We considered theta-gamma coupled rhythms to be preserved (i.e., sufficiently present) if both theta and gamma rhythms had powers that were at least 25% of a reference when STIM was zero (baseline). We quantified theta and gamma powers from the theta-gamma coupled rhythms, and calculated the slope of a linear fit to theta or gamma power plots with STIM. This is illustrated in the *Supplementary Figure* of FIGURE 5. In FIGURE 5, we plot the values of these fitted slopes for each cell type for theta power (**A**), and gamma power (**B**).

We note that theta power increases (i.e., positive values in FIGURE 5**A**) existed only with increas-

ing STIM to PV. PYR and BiC both showed theta power decreases and there was minimal effect with CCK. Considering their medians, maximal absolute changes occurred for PYR and BiC, although BiC showed a large variability. This is statistically significant relative to the other cell types (see TABLE 5). This is interesting since our theoretical analyses above predicted that only PYR+BiC circuits, and not the other two-cell circuit subsystems, produced theta frequency rhythms (see FIGURE 4**G**). Given that our numerical explorations showed that the theta power changed maximally for PYR and BiC when they were stimulated indicates an alignment of the magnitude of theta power change with stimulation in our numerical explorations of the four-cell system with the expression of theta rhythms in our theoretical analyses of the subsystems. For gamma power, the maximal absolute changes occurred for PYR and PV, as shown in FIGURE 5**B**. This is statistically significant for PYR relative to all of the other cell types, and for the PV relative to the other cell types except BiC (see TABLE 5). Given the alignment of the numerics and theory for theta rhythms, our numerical exploration observations suggest that the PYR+PV subsystem could be more key for gamma rhythm generation relative to the CCK+PV subsystem. However, as the gamma powers are much smaller than the theta powers (see *Supplementary Figures* to FIGURE 5), more investigation is needed to extract further particular contributions of cell types for the fast rhythms.

Given the functional importance of theta frequencies, we examined how the theta frequency, as part of the theta-gamma rhythms, changed when the different cell types were stimulated. We quantified how much the theta frequency changed by computing slopes (as illustrated in the *Supplementary Figure* of FIGURE 5). In FIGURE 5**C**, we show this quantification and note that the largest absolute changes occurred with PYR and PV stimulation (see TABLE 6 for statistical significance). BiC showed both increases and decreases in frequency with stimulation.

CCK plays multiple roles in theta-gamma coupled rhythm expression

To assess the susceptibility of each cell type to the expression of theta-gamma coupled rhythms, we measured the range of STIM values associated with sufficient theta-gamma coupling. In FIGURE 5**D**, we present the minimum and maximum STIM values for each cell type. It is evident that CCK exhibits the widest range, indicating that theta-gamma coupled rhythms can be present for a broader spectrum of external inputs compared to the other cell types in the network, with PYR showing the smallest range (see TABLE 5 for statistical significance).

From our degeneracy and connection removal results above, it appears that CCK may have more specific roles compared to other cell types. We thus carried out additional investigations. They revealed that CCK contributes to coupled rhythms in multiple ways. Specifically, CCK is necessary to initiate theta-gamma coupled rhythms from quiescent cellular states, plays a role in regularizing theta rhythms, and can switch theta-gamma coupled rhythms on or off based on its activity level and the activity levels of the other cell types.

We first removed CCK from the four-cell circuit through negative stimulation, either at the beginning of the simulation or during ongoing theta-gamma coupled rhythms in the ten sets (see FIGURE 6, *top, middle plots*). Removal at the start of the simulation *(middle plots)* consistently prevented theta-gamma coupling — note that all cell types begin in a quiescent state across all simulations (see Model and methods section). Introducing a CCK 'burst' to the circuit, previously devoid of theta-gamma coupled rhythms due to the absence of CCK, resulted in the expression of theta-gamma coupling (see FIGURE 6, *middle plots*). Upon examining the timing of CCK and PV following a CCK 'burst,' we find that CCK firing precedes PV firing for all ten sets (not shown). These results strongly support the notion that CCK is central in initiating the expression of theta-gamma coupled rhythms, aligning with our theoretical analyses (see FIGURE 4**H**). However, once coupled rhythms are expressed, CCK activity is not necessarily required. In *Sets 3, 5* (shown in FIGURE 6**B**), and *8*, where CCK activity was needed for the continuation of theta-gamma coupled rhythms, we observe larger connections between PYR and PV (see TABLE 2). This suggests that a sufficiently active PYR can sustain theta-gamma coupled rhythms without CCK activity in the circuit.

We further examined whether there would be any change in the regularity of the ongoing theta

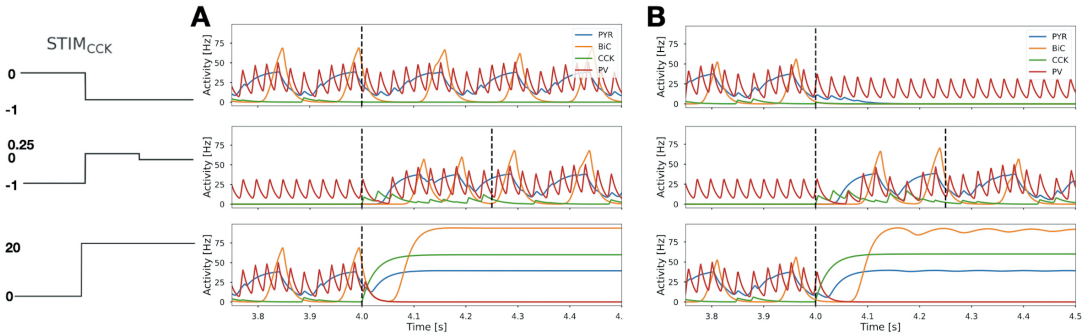

Figure 6. Effects of CCK perturbation on theta-gamma coupled rhythms.
(*Top plots*) CCK is removed from the circuit at 4.0 seconds by changing STIM$_{CCK}$ to -1 (vertical dashed line) leading to continuation of theta-gamma coupled rhythms for *Set 4* (**A**), or to loss of coupled rhythms for *Set 5* (**B**). (*Middle plots*) CCK is removed from the circuit at the start of the simulation, and at 4.0 seconds, CCK is 'added back' to the circuit by changing STIM$_{CCK}$ to 0.25 for a brief interval (as delineated by the vertical dashed lines), and then returned to baseline (i.e., STIM$_{CCK}$ to 0). Theta-gamma coupled rhythms are expressed again. (*Bottom plots*) CCK activity is strongly enhanced in the circuit at 4.0 seconds by changing STIM$_{CCK}$ to 20 (vertical dashed line) leading to loss of theta-gamma coupled rhythms for *Set 4* (**A**), or *Set 5* (**B**). Representation of the changes in STIM$_{CCK}$ are shown on the left hand side for each row of plots.

Figure 6—figure supplement 1. Changes in regularity of theta events.

rhythm with or without CCK during theta-gamma coupled rhythms. Analyzing intervals between PYR peaks (LFP representation), we observed a notable increase in the standard deviation of these intervals when CCK was absent from the circuit producing theta-gamma coupled rhythms in the majority of sets (see TABLE 4 and *Supplementary Figure* of FIGURE 6).

Lastly, strong activation of CCK silences PV, preventing coupled rhythms as gamma rhythms are no longer present in PV and they cannot be propagated to PYR from CCK (see FIGURE 6 (*bottom plots*)). The level of CCK activity, along with the activity of the other cells in the circuit, can serve as a determinant for the expression of theta-gamma coupled rhythms, suggesting a potential 'switching' role for CCK.

Given the functional importance of theta frequencies, we examined how the theta frequency, as part of the theta-gamma rhythms, changed when the different cell types were stimulated. We quantified how much the theta frequency changed by computing slopes (as illustrated in the *Supplementary Figure* of FIGURE 5). In FIGURE 5**D**, we show this quantification and note that the largest absolute changes occurred with PYR and PV stimulation (see TABLE 6 for statistical significance). BiC showed both increases and decreases in frequency with stimulation.

Bringing it all together

Due to the combined insights from our theoretical and numerical analyses of the PRM, we can assign particular roles to the different cell types.

PYR and BiC play the role of theta rhythm generators. This is schematized in FIGURE 7**A**. This is based on the theoretical analyses of the subsystems in which only the PYR+BiC subsystem led to rhythms in the theta frequency band. This was fully supported by the numerical simulations of the full four-cell system that showed that PYR and BiC more strongly affected theta power relative to the other cell types when stimulated. CCK minimally affected the theta power but had an oversized effect on theta-gamma coupled rhythms due its multiple roles described above. Previous numerical studies by (***Chatzikalymniou et al., 2021***) showed that theta rhythms were initiated in large enough PYR networks, which is in line with PYR being key in the theta rhythm portion of the theta-gamma coupled rhythms, both in power and frequency.

CCK contributes to the gamma rhythm portion of theta-gamma coupled rhythms, and our theoretical work indicated that they could serve as 'initiators' of the gamma rhythms, with PV con-

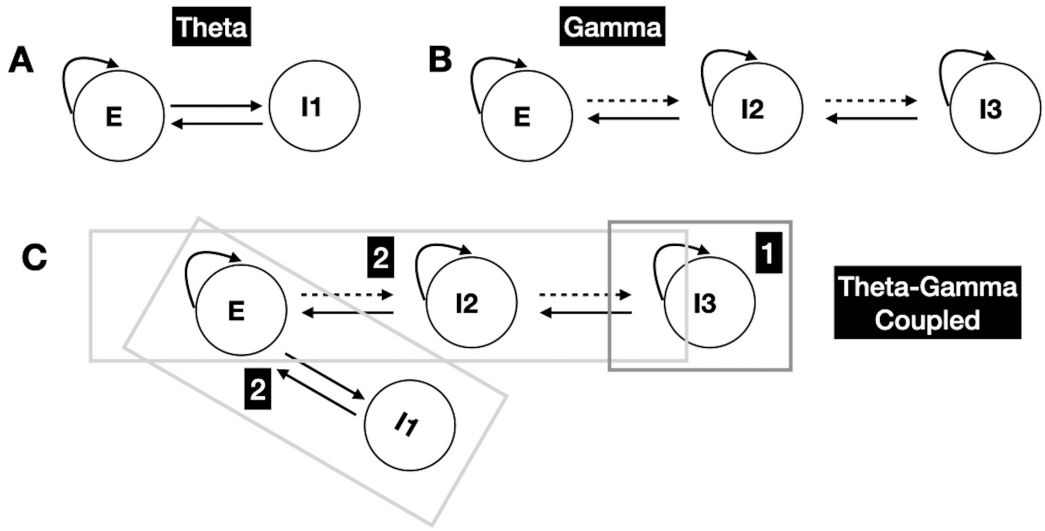

Figure 7. Predicted motifs for coupled rhythms.
As derived from theoretical and numerical analyses of the four-cell circuit shown in FIGURE 1*B* with ***E***=PYR, ***I1***=BiC, ***I2***=PV, ***I3***=CCK. **A** shows the motif for theta rhythm generation, **B** for gamma rhythm generation, and **C** shows the four cell motif for theta-gamma coupled rhythm generation. It occurs in two phases as shown in *C*. In ***phase 1, I3*** initiates the coupled rhythm by being able to disinhibit ***E***, which then allows theta rhythms to be generated (via ***E*** and ***I1***) together with gamma rhythms (via ***E, I1*** and ***I2***) in ***phase 2***. The dashed connection lines means that they are not critical for the system to be able to express theta-gamma coupled rhythms — see TABLE 3. These motifs imply that at least three different inhibitory cell types need to be part of the circuitry for coupled rhythms to be expressed from quiescent states.

Figure 7—figure supplement 1. A blow up of activities to illustrate timings.

tributing to the gamma by 'applying' it to PYR. This is schematized in FIGURE 7**B**. The theory clearly showed that gamma rhythms can emerge from PYR+PV or CCK+PV subsystems. Besides contributing to gamma, the numerical work showed that PV acts as an 'enhancer' of both theta and gamma. That is, it is the only cell type that leads to an increase in both theta and gamma power with increasing stimulation (see FIGURE 5**A,B**). PV also plays a dominant role in controlling the theta frequency — specifically, it leads to decreasing frequency with increasing stimulation.

Given the described roles for the different cell types, we expect that when the PV→PYR connection is removed, there would be no gamma (as it is coming from PV and CCK via PV), and thus no theta-gamma coupled rhythms. However, with removal of the PYR→PV connection type, we expect that theta-gamma coupled rhythms might still be present as theta could still exist due to the PYR+BiC subsystem, and gamma could still 'circulate', as schematized in FIGURE 4**H**. In TABLE 3, we see that theta-gamma coupled rhythms can be present for some of the parameter sets.

CCK has multiple roles in the existence of theta-gamma coupled rhythms. However, it does not play a key role in theta frequency control or of theta power (relative to the other cell types). By design, theta is not present with the removal of the CCK→PV connection (see FIGURE 2**D**), but a small gamma remains that would be due to PV. Theta-gamma coupled rhythms can remain when the PV→CCK connection is removed. This makes sense since CCK would still be able to initiate the coupled rhythms. If PYR, PV and BiC cells are quiescent, or not active enough, CCK is needed to initiate theta-gamma coupled rhythms. But it is possible that CCK is not needed to maintain theta-gamma coupled rhythms if the different cells' histories are such that they are active enough. However, CCK clearly contributes to the regularity of the theta rhythm would be less regular (see TABLE 4).

We thus present a two-phase process for the generation of theta-gamma coupled rhythms in the hippocampus, as schematized in FIGURE 7**C**. In the first phase, CCK generates gamma rhythms

to initiate the theta-gamma coupled rhythm process. It can do this prior to PV contributing to gamma rhythms in light of its intrinsic properties (higher input resistance) and its surrounding milieu (see *Supplementary Figure* of FIGURE 2). The *Supplementary Figure* of FIGURE 7 shows examples from two of the parameter sets illustrating CCK peaking before PV. In the second phase, theta is generated (by PYR and BiC) and gamma is enhanced (by PYR and PV), leading to theta-gamma coupled rhythms. In essence, the disinhibitory effect of CCK to PYR plays a controlling role in the two-phase process. Overall, we suggest that the following motifs shown in FIGURE 7 underlie theta-gamma coupled rhythms, and could serve as a motif 'template' for the existence of coupled rhythms of high and low frequencies in the brain.

Discussion

Summary and predictions

Combining theoretical and numerical insights of a four-cell circuit model of CA1 hippocampus, we showed that different inhibitory cell types contribute to theta-gamma coupled rhythms in particular ways. The theoretical analyses showed that theta rhythms originate in PYR+BiC circuits, but neither in PV+PYR nor in CCK+PV circuits. For gamma rhythms, PYR+PV or CCK+PV circuits could be responsible, but not PYR+BiC circuits on their own. Systematic numerical explorations supported the prediction that PYR and BiC underlie theta rhythm generation as they showed the largest modulation in theta power when stimulated. We note that the theoretical work was done considering the three possible two-cell circuit motifs and the numerical explorations were done with the full four-cell circuits expressing theta-gamma coupled rhythms. However, considering the combination and consistency of the theoretical and numerical results involving particular cell types, we predict that PYR and BiC are the main cell types in the circuit required to generate theta rhythms. This suggests that without BiC, *robust* theta rhythms, as part of theta-gamma coupled rhythms, would not occur. As BiC and PV are both PV-expressing type cells, this indicates that one should probably not consider PV-expressing cell types in a lumped functional fashion. For example, the distinctiveness of another PV-expressing cell type, chandelier cells, is fully appreciated from functional perspectives (***Compans and Burrone, 2023***). However, specific functional differentiation of PV-expressing bistratified and basket cells has not been reported, although anatomical differences are well-described (***Müller and Remy, 2014***).

It is known that CCK is a cell type that is highly modulated (***Freund and Katona, 2007***). In particular, it is known that CCK expresses highly asynchronous postsynaptic potentials (***Daw et al., 2009***) making it notable that we found that the CCK→PV connection type has a higher standard deviation relative to other connection types (see FIGURE 3**B**). From our theoretical work using two-cell subsystems, we had suggested that CCK initiated gamma rhythms. From our numerical explorations, we found that CCK was needed to initiate theta-gamma coupled rhythms from quiescent states. Recent experimental studies have shown alternating sources of perisomatic inhibition onto pyramidal cells during behaviour via CCK-expressing and PV-expressing basket cells involving inhibitory mechanisms between these cell types (***Dudok et al., 2021***). Theta-gamma coupled rhythms are expressed during movement exploration and REM sleep (***Buzsaki, 2011***), and thus, it would be interesting to examine whether these coupled rhythms are differentially affected by perturbing either PV-expressing or CCK-expressing basket cells, and whether CCK-expressing basket cells play a more robust role relative to other inhibitory cell types in the expression of theta-gamma coupled rhythms. Our results here predict that the removal of CCK-expressing basket cells should drastically reduce the presence of theta-gamma coupled rhythms although perhaps not eradicate it, and the regularity of the theta rhythms should be reduced. Further, we predict that modulation of CCK-expressing basket cells could lead to theta-gamma coupled rhythms being turned on or off, thus acting to control the 'mood' (as borrowed from ***Freund*** (***2003***) terminology) of the system.

Whereas PYR and BiC were the main cell types associated with theta rhythm generation in our model, PYR and PV showed the most modulation when theta frequency was considered (see

FIGURE 5**C**). In earlier work using detailed CA1 circuit models, we had shown that large enough networks of PYR were required to initiate theta rhythms, and inhibitory cell populations 'regularized' the rhythm, which we termed an 'inhibition-based tuning' mechanism (***Chatzikalymniou et al., 2021***; ***Skinner et al., 2021***). We also found that inputs to PYR were able to set the population theta rhythm frequency, increasing with larger net excitatory drive. Our PRM results here are entirely consistent with the results obtained using these more detailed circuit models. That is, we found that theta frequency is most strongly affected by PYR stimulation, increasing when PYR were stimulated, that is, an increased net excitatory drive (see FIGURE 5**C**).

Related studies

For gamma rhythms, ING (interneuron network gamma) and PING (pyramidal interneuron network gamma) mechanisms have been proposed (***Whittington et al., 2000***). Our theoretical work here pointed to either PYR and PV or CCK and PV circuits as the gamma generators. Further, removal of PV→PV or PV→PYR connections abolished gamma rhythms. On the surface, this would indicate support for a PING mechanism. However, we note that in the biological system, it is perhaps not so much about whether the gamma rhythm is generated by PING or ING mechanisms per se, but rather, what and how the different cell type involvements come about. PING and ING certainly help us think about what sort of excitatory and inhibitory balances might be key, but distinct cell types and the co-modulated oscillation considerations here supersede these classical ING and PING ideas. Naturally, what ultimately matters is what experiments can be done to differentiate and understand the contributions from the various excitatory and inhibitory cell types and their interactions in producing the circuit output, such as was considered for visual cortex (***Tiesinga and Sejnowski, 2009***). Here, using a mean field model with distinct cell types, our theoretical and numerical analyses allowed us to present circuit motifs that could underlie the co-expression of high and low frequency rhythms. In particular, gamma rhythms involve a three-cell motif in this co-expression (FIGURE 7).

A recent data-driven modeling study probed theta-gamma phase amplitude coupling (PAC) in hippocampal circuits focusing on three cell types - pyramidal cells, PV-expressing basket cells and oriens-lacunosum-moleculare (OLM) cells (***Ponzi et al., 2023***). Multi-compartment detailed cellular models were used along with short-term synaptic plasticity, allowing the authors to highlight these cell types and particular aspects. Their results indicated a dependence of theta oscillation expression on gamma for the ubiquity of PAC output via these cell types and their interconnections. Specifically, they showed that the theta rhythm frequency and strength relied on a PING mechanism. Our PRM is supportive of PING and is thus consistent with ***Ponzi et al.*** (***2023***). However, we did not apply PAC measures to our LFP representations in the PRM.

Due to the identification of connections between bistratified and OLM cells (***Leão et al., 2012***), we had previously undertaken modeling studies to examine their interacting contributions to theta rhythms in LFP recordings (***Chatzikalymniou and Skinner, 2018***; ***Ferguson et al., 2015***). We found that bistratified cell innervation of pyramidal cells, but not OLM cells, was an essential contribution for LFP theta expression. In light of our results here identifying pyramidal and bistratified cells as a key circuit for LFP theta rhythm generation, this is an interesting overlap, although it should not be overly emphasized as the underlying mathematical model and their explorations were quite different. The PRM examined theta and gamma generation in a theta-gamma coupled rhythm context, whereas these other studies were focused on theta rhythm generation in biophysical LFP models using volume conductor theory.

Distinct cell types

The plethora of various inhibitory cell types with their particular biophysical characteristics and connectivities in the hippocampus (***Pelkey et al., 2017***) make it challenging to figure out their particular contributions to dynamic network oscillations in the behaving animal. However, as theta-gamma coupled rhythms reflect cognitive processing and are potential disease biomarkers, *and* involve the

various inhibitory cell types, we cannot ignore the potential roles played by these different types of interneurons. Such considerations led us to here using mean field models with distinct cell types and interconnections.

The distinctness of interneurons is being unravelled by use of new technologies and combinations (***Gouwens et al., 2020***; ***Harris et al., 2018***), as well as revealing distinct cell type similarities between hippocampus and isocortex (***Yao et al., 2021***). There are putatively 28 well-defined types that are within somatostatin (13), parvalbumin (5), Lamp5 (2), Sncg (3) and vasoactive intestinal polypeptide (VIP) (5) types. Close consideration indicates that bistratified and PV-expressing basket cells (within parvalbumin type), and CCK-expressing basket cells (within Sncg type) are clearly distinguishable. Thus, the cell types within the four-cell circuit are distinct making any obtained cellular-based insights meaningful from a biological cell-type perspective. Specifically, as described above, we found differential contributions of bistratified and PV-expressing basket cells regarding theta rhythms.

The relative strength of connections between inhibitory populations seems to change across the septo-temporal axis of the CA1 hippocampus and across layers (***Soltesz and Losonczy, 2018***; ***Navas-Olive et al., 2020***). ***Navas-Olive et al.*** (***2020***) have shown that PV-expressing basket cells preferentially innervate pyramidal cells at the deep sublayers while CCK-expressing basket cells are more likely to target the superficial pyramidal cells. Also, there is different innervation of pyramidal cells by bistratified and OLM cells for deep versus superficial pyramidal cells. We can start to consider how these differential connectivities affect theta-gamma coupled rhythm control by focusing on such perturbations in the PRM. Interestingly, we note that when connections from PV-expressing basket cells to pyramidal cells are larger (smaller), there is a smaller (larger) theta frequency (see TABLE 2), suggesting theta frequency differences between deep and superficial layers due to particular connection weight differences.

Limitations and future work

Several biological aspects are not directly represented in the PRM. This includes aspects such as spatial inhibitory distributions and inputs onto pyramidal cells, short-term plasticity as well as the inclusion of additional inhibitory cell types. The results from our study do not of course imply that these other aspects are not important. Rather, our results are limited by the cell types and interconnections that were included (FIGURE 1). It may be possible to use our existing PRM as a starting base to consider additional cell type contributions. For example, the contribution of OLM cells could be initially considered in an indirect way through its effect on bistratified cells by considering a decreasing STIM (inhibitory input) onto them - the PRM would indicate an enhanced theta power (see FIGURE 5**A**). Specific known motifs that include VIP-expressing cell types (***Guet-McCreight et al., 2020***) can also be considered indirectly. Interneuron-specific 3 cells (VIP-expressing subtype) are known to differentially inhibit OLM cells, bistratified and basket cells (***Tyan et al., 2014***), and so an initial consideration of inputs received by these different cell types and their effect on theta-gamma coupled rhythms could be probed. Also, as theta frequency and behavioural correlates are known to vary across the dorsoventral axis (***Strange et al., 2014***), we can consider leveraging our models to understand these differences from particular cell types and interconnection variations. In general, one could envision expanding the PRM to directly include additional cell type populations and connectivities and interpretations to develop further hypotheses and obtain predictions for experimental examination.

For the PRM used here, despite our experimental linkage of each cell type's intrinsic excitability, further examination of the different parameters is warranted. For example, different and differential β's and delays could be considered to better capture the different cell types, and the formal inclusion of synaptic time constants could be considered. Additional theoretical analyses may be possible, but here we were able to exploit bifurcation analyses to extract our insights. Finally, it may be interesting to explore neurostimulation protocols with the PRM for experimental linkage design considerations.

Model and methods

The population rate model (PRM)

The purpose of the PRM is the identification and analysis of key mechanisms involved in the generation and control of theta-gamma coupled rhythms, that is, coupling interactions between theta and gamma rhythms, in hippocampal microcircuits, following the formalism of population-scale mean-field models. The PRM describes the time evolution of PYR, BiC, CCK, and PV activities or mean firing rates ($r_{PYR}, r_{BiC}, r_{CCK}$ and r_{PV}) as a function of their mutual connectivity motif (FIGURE 1), synaptic weights ($w_{n\to m}$, for n, m = PYR, BiC, CCK, PV), membrane rate constants ($\alpha_{PYR}, \alpha_{BiC}, \alpha_{CCK}$ and α_{PV}), synaptic and axonal delays lumped in a single term (τ), cell-specific intrinsic excitability (ie), and how these collectively contribute to the generation of rhythmic firing rate expression. The resulting model builds on the well-known (***Wilson and Cowan, 1972***) formalism, resulting in the following set of nonlinear, delayed differential equations,

$$\alpha_{PYR}^{-1}\frac{dr_{PYR}}{dt}(t) = -r_{PYR}(t) + r_{0,PYR} f[I_{PYR}^{\tau}(t)] \tag{1a}$$

$$\alpha_{BiC}^{-1}\frac{dr_{BiC}}{dt}(t) = -r_{BiC}(t) + r_{0,BiC} f[I_{BiC}^{\tau}(t)] \tag{1b}$$

$$\alpha_{CCK}^{-1}\frac{dr_{CCK}}{dt}(t) = -r_{CCK}(t) + r_{0,CCK} f[I_{CCK}^{\tau}(t)] \tag{1c}$$

$$\alpha_{PV}^{-1}\frac{dr_{PV}}{dt}(t) = -r_{PV}(t) + r_{0,PV} f[I_{PV}^{\tau}(t)] \tag{1d}$$

where $r_{0,m}$ (here and below, m = PYR, BiC, CCK or PV) represents the maximal firing rate of the neurons. Fluctuations in mean firing rates result from the nonlinear integration of presynaptic inputs I_m.

Presynaptic inputs I_m scale firing rates through the firing rate response function

$$f[I_m] = \frac{1}{1 + e^{-\beta(ie_m + I_m)}} \tag{2}$$

whose gain β reflects the steepness of the response, and intrinsic excitability (ie_m) allows cell-specific threshold, rheobase, and input resistances to be taken into consideration. The presynaptic inputs for the four cell types considered are given by

$$I_{PYR}^{\tau}(t) = w_{PYR\to PYR}\, r_{PYR}^{\tau} \;+\; w_{BiC\to PYR}\, r_{BiC}^{\tau} + \; w_{PV\to PYR}\, r_{PV}^{\tau} \;+\; STIM_{PYR} \tag{3a}$$

$$I_{BiC}^{\tau}(t) = w_{PYR\to BiC}\, r_{PYR}^{\tau} \;+\; STIM_{BiC} \tag{3b}$$

$$I_{CCK}^{\tau}(t) = w_{CCK\to CCK}\, r_{CCK}^{\tau} \;+\; w_{PV\to CCK}\, r_{PV}^{\tau} + \; STIM_{CCK} \tag{3c}$$

$$I_{PV}^{\tau}(t) = w_{CCK\to PV}\, r_{CCK}^{\tau} \;+\; w_{PV\to PV}\, r_{PV}^{\tau} + \; w_{PYR\to PV}\, r_{PYR}^{\tau} \;+\; STIM_{PV} \tag{3d}$$

where $r_m^{\tau} = r_m(t-\tau)$. A time delay of $\tau = 5$ ms is included to represent physiological axon conduction delays and synaptic activation time values. The α_m parameter sets the time scale at which populations respond to stimuli. Cell-specific sensitivities and control are explored by including an additional input ($STIM_m$).

Choosing the initial PRM parameter set

Based on the experimental literature, we set parameter values for membrane rate constants (α's) and maximal firing rates (r_o's) of the different cell types. β and τ values were fixed reasonably, and β was set to the same value for all cell types. We obtained ie's for the different cell types and a set of synaptic weights (see TABLE 1 and see *Set 0* in TABLE 2) that allowed the system to produce theta-gamma coupled rhythms. The experimental literature resources were derived from online databases (***Wheeler et al., 2015***) and Table 6 and Appendix 1 of (***Bezaire et al., 2016***). The resulting intrinsic activities (i.e., when all synaptic weights are zero) are shown in *Supplementary Figure* of FIGURE 2, where the different maximal firings and differential STIM responses (considering rheobase and input resistance values) are consistent with the literature. Note that zero synaptic weights here

Table 1. Parameter Values for PRM

Symbol	Definition	Value
β	Response function gain	20 au
τ	delay	5 ms
α_{PYR}	PYR rate constant	40 Hz
α_{BiC}	BiC rate constant	80 Hz
α_{CCK}	CCK rate constant	40 Hz
α_{PV}	PV rate constant	80 Hz
ie_{PYR}	PYR intrinsic excitability	0.03 au
ie_{BiC}	BiC intrinsic excitability	-1.45 au
ie_{CCK}	CCK intrinsic excitability	0.8 au
ie_{PV}	PV intrinsic excitability	0.5 au
$r_{0,PYR}$	PYR maximal firing rate	40 Hz
$r_{0,BiC}$	BiC maximal firing rate	100 Hz
$r_{0,CCK}$	CCK maximal firing rate	60 Hz
$r_{0,PV}$	PV maximal firing rate	100 Hz

do not prevent an interpretation that the different cell types receive inputs from other sources, just not from the other cell types included here.

Simulations

Simulations of the PRM were performed using an Euler method to numerically integrate the differential equations with a time-step of 0.001 seconds. Each simulation was performed for 8.0 seconds. The initial conditions were set to zero for all cell types. The first second of the simulations was not used in the spectral analysis to avoid the transients at the start of the simulations from affecting the analysis. The output of these simulations contains the activity of the four cell types in the model. These represent the population firing rate for the corresponding cell type.

Frequency bands and power spectral density (PSD)

We define the low-frequency *theta* band to be between 3-12 Hz and the high-frequency *gamma* band to be between 20-100 Hz. We used a Welch periodogram of the signal and separated it into the two frequency bands. The dominant frequency and its corresponding power were calculated as the frequency where the highest peak appears in each frequency band and the power spectral density (PSD) at that frequency.

We found that filtering the signal into the low and high frequency bands caused anomalies due to the harmonics of the theta signal having a higher power than the gamma signal for PYR. This is due to the large difference in power between the theta and gamma bands in PYR activity. To circumvent the issue where the harmonics of PYR theta activity were stronger than PYR gamma activity, we used the periodogram of PV activity to find where the dominant frequency in the gamma band was present. This was done because PV activity has a stronger gamma component and as such, the harmonics of its activity in the theta band do not produce spurious results. Using the dominant frequency in the gamma band that we derived from the periodogram of PV activity, we find the corresponding PSD for PYR at that frequency to calculate the PSD in the gamma band.

We interpret PYR as an analog of the LFP because of the much larger prevalence of PYR compared to all the other cells in the network in actual brain tissue and that LFP recordings occur in the pyramidal cell layer where PYR cell bodies are located. The average theta and gamma powers from the ten selected parameter sets (see TABLE 2) were used as a reference to determine whether simulation outputs had theta and gamma rhythms of a considerable enough power. Oscillations were considered 'sufficient' if both the theta and gamma power were at least 25% of this reference.

Considering both theta and gamma powers in this way ensured that co-expression was reasonably present, as would be reflected in a ratio of the two powers. Performing more sophisticated analyses of cross-frequency coupling (CFC) was not deemed appropriate for these model LFP signals as the type of CFC could take many forms such as phase-amplitude coupling (PAC), phase-phase or amplitude-amplitude coupling, and details of the signal shape, for example, could produce many confounds (***Scheffer-Teixeira and Tort, 2022***).

Hypotheses testing and genetic algorithm

Using the initial set of synaptic weights (*Set 0*) to start, a genetic algorithm was used to explore the parameter space of the nine synaptic weights and find additional sets of synaptic weights that would produce theta-gamma coupled rhythms satisfying our hypotheses and experimental constraints.

A given set of synaptic weights must satisfy the following constraints:

- Primary: At baseline (i.e., no connections removed, and no STIM applied), the system should exhibit theta and gamma oscillations such that:
  - the power of PYR at the most prominent frequency in the theta and gamma bands are at least 60% of that in *Set 0*.
  - the ratio of the maximal firing rate (i.e., activity) for PV and BiC is at least 0.67
  - the maximal firing rate of CCK is greater than 4
- Secondary: When a certain connection type is removed, the theta oscillations break down.
  - These connection types are: PYR→PYR, CCK→PV, PV→PYR, and BiC→PYR.
  - This is quantified by the power of the most prominent frequency in the theta band for PYR being less than 10% of that in *Set 0* at baseline.

Using our genetic algorithm, we 'mutated' the synaptic weights of a constrained parameter set and checked if the resultant new set satisfied our hypotheses. If a new set does satisfy all the hypotheses, it is added to the list of the constrained sets for the next iteration of mutations. This was continued until a target number of constrained sets was found — that we set to be 200 — or a maximum number of iterations were completed

The resulting parameter sets were then clustered in the w parameter space using a *k-means* clustering algorithm (***Pedregosa et al., 2011***). We found 13 distinct clusters from the 200 parameter sets. To reduce this, we decided to only analyze the clusters where at least one set of synaptic weights produced oscillations where the ratio of the activities of PV and BiC was at least 0.70 — that is, increased from 0.67 used in the primary constraints. This ratio is based on relative firing rates presented in Table 6 of ***Bezaire et al.*** (***2016***), and the firing rate for CCK was chosen to ensure its participation in the overall system (as noted from multiple simulations). Using this additional threshold, we discarded three of the clusters that we had found. The ratios and CCK activities for these sets are given in TABLE 2.

Varying STIM

To explore how each cell type would respond when perturbed, stimulation (STIM) applied to each cell type was varied as a form of sensitivity analysis. Specifically, the STIM to each cell type was varied between -2 and 2, keeping the STIM to all other cell types fixed at zero. A positive value of STIM would mean that a cell type was being excited more than at baseline (where no STIM is applied) while a negative value of STIM would mean that the cell type is inhibited more than at baseline.

We used 121 equally spaced points in the range of values we explored. At each STIM value, the PRM was simulated and the theta frequency, theta power, and gamma power of PYR activity (i.e., LFP output representation) was calculated. A line of best fit was calculated for each of theta

frequency, theta power and gamma power to quantify their change with respect to STIM to a particular cell type. The STIM range was considered as the difference between the largest and smallest STIM values that produced sufficient oscillations. Only points that showed sufficient oscillations (see above) were used for these calculations.

Testing for regularization

The system was simulated for a total of ten seconds, with the same time-step as previously used. For the first five seconds, STIM to all cell types was set to zero. At t = 5 seconds, STIM$_{CCK}$ = -1 was applied to silence CCK. The recording was split into two sections of four seconds each: the section from t = 1-5 seconds when CCK is active and the section from t = 6-10 seconds when CCK is silent. The first one second interval after the start of the simulation and after STIM$_{CCK}$ = -1 was applied is ignored to not count any transient activity in the analysis. For each section, the peaks in the PYR and BiC activity were recorded. The mean, median, and standard deviation of the amplitudes of the peaks and the inter-spike interval (ISI) were recorded. This procedure was performed for all parameter sets where applicable.

Linear stability analysis

For the analysis we switch to the following notation: the mean firing rates r_{PYR}, r_{BiC}, r_{CCK} and r_{PV} will be denoted by x_1, x_2, x_3 and x_4, respectively. The maximal firing rates $r_{0,PYR}$, $r_{0,BiC}$, $r_{0,CCK}$ and $r_{0,PV}$ will be denoted by r_1, r_2, r_3 and r_4, respectively. To understand the mechanism of PRM we break it into three subsystems: PYR+BiC, PYR+PV and CCK+PV. The first considers the dynamics of PYR and BiC cells:

$$\frac{d}{dt}x_1(t) = \alpha_{PYR}(-x_1(t) + r_1 f[I^{\tau}_{PYR}(t)]) \tag{4a}$$

$$\frac{d}{dt}x_2(t) = \alpha_{BiC}(-x_2(t) + r_2 f[I^{\tau}_{BiC}(t)]) \tag{4b}$$

where I^{τ}_{PYR} is as in Eq. (3a) with $w_{PV\to PYR} = 0$ and I^{τ}_{BiC} is as in Eq. (3b). The second one considers the dynamics of PYR and PV:

$$\frac{d}{dt}x_1(t) = \alpha_{PYR}(-x_1(t) + r_1 f[I^{\tau}_{PYR}(t)]) \tag{5a}$$

$$\frac{d}{dt}x_4(t) = \alpha_{PV}(-x_4(t) + r_4 f[I^{\tau}_{PV}(t)]) \tag{5b}$$

where I^{τ}_{PYR} and I^{τ}_{PV} are defined as in Eq. (3a) and Eq. (3d), respectively, with $w_{BiC\to PYR} = 0$ and $w_{CCK\to PV} = 0$. The third subsystem considers the dynamics of PV and CCK, and is given by:

$$\frac{d}{dt}x_3(t) = \alpha_{CCK}(-x_3(t) + r_3 f[I^{\tau}_{CCK}(t)]) \tag{6a}$$

$$\frac{d}{dt}x_4(t) = \alpha_{PV}(-x_4(t) + r_4 f[I^{\tau}_{PV}(t)]) \tag{6b}$$

where I^{τ}_{CCK} and I^{τ}_{PV} are defined as in Eq. (3c)-(3d), respectively, with $w_{PYR\to PV} = 0$.

We start the analysis with the system of Eqs. (4a)-(4b). The point (x_1^*, x_2^*) is an equilibrium point of Eqs. (4a)-(4b) if there is a solution to

$$ie_{PYR} = f^{-1}[r_1^{-1}x_1^*] - w_{PYR\to PYR}\, x_1^* - w_{BiC\to PYR}\, x_2^* \tag{7a}$$

$$ie_{BiC} = f^{-1}[r_2^{-1}x_2^*] - w_{PYR\to BiC}\, x_1^*, \tag{7b}$$

where $f^{-1}(y) = \beta^{-1}\ln(y/(1-y))$. Note that we have dropped the additional inputs $STIM_{PYR}$ and $STIM_{BiC}$ from Eqs. (7a)-(7b) as they were initially considered to be zero.

Denote the right hand side of Eq. (4a) by $\phi(x_1, x_2)$, and of Eq. (4b) by $\chi(x_1, x_2)$. Linearizing Eqs. (4a)-(4b) around the equilibrium point (x_1^*, x_2^*) we find the Jacobian matrix

$$\begin{pmatrix} \frac{\partial\phi}{\partial x_1} & \frac{\partial\phi}{\partial x_2} \\ \frac{\partial\chi}{\partial x_1} & \frac{\partial\chi}{\partial x_2} \end{pmatrix}. \tag{8}$$

The first-order partial derivatives of the above matrix are

$$\begin{aligned}
\frac{\partial \phi}{\partial x_1} &= -\alpha_{PYR} + \alpha_{PYR}\,\beta\, w_{PYR\to PYR}\, x_1^*\,(1 - r_1^{-1} x_1^*) := \alpha_{PYR}(-1+\gamma_{11}) \\
\frac{\partial \phi}{\partial x_2} &= \alpha_{PYR}\,\beta\, w_{BiC\to PYR}\, x_1^*\,(1 - r_1^{-1} x_1^*) := \alpha_{PYR}\gamma_{12} \\
\frac{\partial \chi}{\partial x_1} &= \alpha_{BiC}\,\beta\, w_{PYR\to BiC}\, x_2^*\,(1 - r_2^{-1} x_2^*) := \alpha_{BiC}\gamma_{21} \\
\frac{\partial \chi}{\partial x_2} &= -\alpha_{BiC}\,.
\end{aligned}$$

The solution of the linearized system is of the form $(x_1(t), x_2(t)) = (c_1, c_2)e^{\lambda t}$ where c_1, c_2 are nonzero constants, λ are the eigenvalues and $t > 0$. A condition on λ is given by the equation

$$D(\lambda) = 0\,, \tag{9}$$

where

$$D(\lambda) = det\begin{pmatrix} \lambda + \alpha_{PYR} - \alpha_{PYR}\gamma_{11}e^{-\lambda\tau} & -\alpha_{PYR}\gamma_{12}e^{-\lambda\tau} \\ -\alpha_{BiC}\gamma_{21}e^{-\lambda\tau} & \lambda + \alpha_{BiC} \end{pmatrix}. \tag{10}$$

From Eq. (9) we have

$$\lambda^2 + (\alpha_{PYR} + \alpha_{BiC})\lambda + \alpha_{PYR}\alpha_{BiC} + (-\alpha_{PYR}\gamma_{11}\lambda - \alpha_{PYR}\alpha_{BiC}\gamma_{11})e^{-\lambda\tau} - \alpha_{PYR}\alpha_{BiC}\gamma_{12}\gamma_{21}e^{-2\lambda\tau} = 0\,.$$

To simplify the above expression we multiply by $e^{\lambda\tau}$:

$$(\lambda^2 + (\alpha_{PYR} + \alpha_{BiC})\lambda + \alpha_{PYR}\alpha_{BiC})e^{\lambda\tau} - \alpha_{PYR}\gamma_{11}\lambda - \alpha_{PYR}\alpha_{BiC}\gamma_{11} - \alpha_{PYR}\alpha_{BiC}\gamma_{12}\gamma_{21}e^{-\lambda\tau} = 0\,. \tag{11}$$

If $\lambda = i\omega$, for ω a nonzero real number, the bifurcation condition is defined by the simultaneous solution of the equations $\mathrm{Re}(D(i\omega)) = 0$ and $\mathrm{Im}(D(i\omega)) = 0$. Substituting $\lambda = i\omega$ into Eq. (11) we conclude that the real and imaginary parts are:

$$\mathrm{Re}(D(i\omega)) = (-\omega^2 + \alpha_{PYR}\alpha_{BiC}(1 - \gamma_{12}\gamma_{21}))\cos(\omega\tau) - (\alpha_{PYR} + \alpha_{BiC})\omega\sin(\omega\tau) - \alpha_{PYR}\alpha_{BiC}\gamma_{11} \tag{12}$$

and

$$\mathrm{Im}(D(i\omega)) = (-\omega^2 + \alpha_{PYR}\alpha_{BiC}(1 + \gamma_{12}\gamma_{21}))\sin(\omega\tau) + (\alpha_{PYR} + \alpha_{BiC})\omega\cos(\omega\tau) - \alpha_{PYR}\gamma_{11}\omega\,. \tag{13}$$

Taking $\mathrm{Re}(D(i\omega)) = 0$ and $\mathrm{Im}(D(i\omega)) = 0$ we find

$$\begin{aligned}
\kappa_1\cos(\omega\tau) + \kappa_2\sin(\omega\tau) + \kappa_3 = 0 \\
\kappa_4\cos(\omega\tau) + \kappa_5\sin(\omega\tau) + \kappa_6 = 0
\end{aligned} \tag{14}$$

where we have further simplified the notation as follows:

$$\begin{aligned}
&\kappa_1 := -\omega^2 + \alpha_{PYR}\alpha_{BiC}(1 - \gamma_{12}\gamma_{21}), \quad \kappa_2 := -(\alpha_{PYR} + \alpha_{BiC})\omega, \quad \kappa_3 := -\alpha_{PYR}\alpha_{BiC}\gamma_{11}, \\
&\kappa_4 := (\alpha_{PYR} + \alpha_{BiC})\omega, \quad \kappa_5 := -\omega^2 + \alpha_{PYR}\alpha_{BiC}(1 + \gamma_{12}\gamma_{21}), \quad \kappa_6 := -\alpha_{PYR}\gamma_{11}\omega\,.
\end{aligned} \tag{15}$$

From Eq. (14) we have that

$$\sin(\omega\tau) = \frac{\kappa_3\kappa_4 - \kappa_1\kappa_6}{\kappa_1\kappa_5 - \kappa_2\kappa_4} := G_1(\omega) \tag{16a}$$

$$\cos(\omega\tau) = \frac{\kappa_2\kappa_6 - \kappa_3\kappa_5}{\kappa_1\kappa_5 - \kappa_2\kappa_4} := G_2(\omega)\,. \tag{16b}$$

Notice that G_1 and G_2 depend only on ω, hence solving Eqs. (16a)-(16b) with respect to ω we are able to find the frequency. Indeed, the trigonometric equation $\sin^2(\omega\tau) + \cos^2(\omega\tau) = 1$ implies that $G_1^2(\omega) + G_2^2(\omega) = 1$. Solving the latter equation with parameter values of *Set 0* we found a frequency in the theta band. From Eq. (16a) we may also calculate the delay τ as follows:

$$\tau^k = \frac{1}{\omega}(\arcsin(G_1(\omega)) + 2k\pi), \quad k = 0, 1, 2, \dots\ . \tag{17}$$

The smallest such value is the first bifurcation point.

We repeat the same steps as above for the stability analysis of the two other subsystems (PYR+PV and CCK+PV). In FIGURE 4G, we plot the bifurcation points (coloured triangles) for each of the three subsystems. For delays smaller than the critical ones the subsystems are either stable or oscillations are damping. For delays larger than the critical ones the oscillations are periodic. The curves plotted in FIGURE 4G are approximations of the frequencies at given delays, as computed by Eq. (17).

Acknowledgments

This research was supported by the Natural Sciences and Engineering Research Council of Canada (NSERC) Discovery grants to FKS and JL.

References

Bandarabadi M, Boyce R, Gutierrez Herrera C, Bassetti CL, Williams S, Schindler K, Adamantidis A. Dynamic modulation of theta-gamma coupling during rapid eye movement sleep. Sleep. 2019 Dec; 42(12). doi: 10.1093/sleep/zsz182.

Bezaire MJ, Raikov I, Burk K, Vyas D, Soltesz I. Interneuronal mechanisms of hippocampal theta oscillation in a full-scale model of the rodent CA1 circuit. eLife. 2016 Dec; 5:e18566. doi: 10.7554/eLife.18566.

Buzsaki G. Hippocampus. Scholarpedia. 2011; 6(1):1468. http://www.scholarpedia.org/article/Hippocampus, doi: 10.4249/scholarpedia.1468.

Buzsáki G. Rhythms of the Brain. 1 ed. Oxford University Press, USA; 2006.

Buzsáki G. Theta oscillations in the hippocampus. Neuron. 2002 Jan; 33(3):325–340. http://www.ncbi.nlm.nih.gov/pubmed/11832222.

Buzsáki G, Moser EI. Memory, navigation and theta rhythm in the hippocampal-entorhinal system. Nature neuroscience. 2013 Jan; 16(2):130–138. doi: 10.1038/nn.3304.

Chatzikalymniou AP, Sengupta S, Lefebvre J, Skinner FK. Cholecystokinin-expressing (CCK+) basket cells are key controllers of theta-gamma coupled rhythms in the hippocampus. bioRxiv. 2022 Sep; doi: 10.1101/2022.06.01.494440, pages: 2022.06.01.494440 Section: New Results.

Chatzikalymniou AP, Skinner FK. Deciphering the Contribution of Oriens-Lacunosum/Moleculare (OLM) Cells to Intrinsic θ Rhythms Using Biophysical Local Field Potential (LFP) Models. eNeuro. 2018 Jul; 5(4):ENEURO.0146–18.2018. doi: 10.1523/ENEURO.0146-18.2018.

Chatzikalymniou AP, Gumus M, Skinner FK. Linking minimal and detailed models of CA1 microcircuits reveals how theta rhythms emerge and their frequencies controlled. Hippocampus. 2021; 31(9):982–1002. doi: 10.1002/hipo.23364.

Colgin LL. Theta–gamma coupling in the entorhinal–hippocampal system. Current Opinion in Neurobiology. 2015 Apr; 31:45–50. doi: 10.1016/j.conb.2014.08.001.

Colgin LL. Rhythms of the hippocampal network. Nature Reviews Neuroscience. 2016 Apr; 17(4):239–249. doi: 10.1038/nrn.2016.21.

Compans B, Burrone J. Chandelier cells shine a light on the formation of GABAergic synapses. Current Opinion in Neurobiology. 2023 Jun; 80:102697. doi: 10.1016/j.conb.2023.102697.

Daw MI, Tricoire L, Erdelyi F, Szabo G, McBain CJ. Asynchronous Transmitter Release from Cholecystokinin-Containing Inhibitory Interneurons Is Widespread and Target-Cell Independent. The Journal of Neuroscience. 2009 Sep; 29(36):11112–11122. doi: 10.1523/JNEUROSCI.5760-08.2009.

Dudok B, Klein PM, Hwaun E, Lee BR, Yao Z, Fong O, Bowler JC, Terada S, Sparks FT, Szabo GG, Farrell JS, Berg J, Daigle TL, Tasic B, Dimidschstein J, Fishell G, Losonczy A, Zeng H, Soltesz I. Alternating sources of perisomatic inhibition during behavior. Neuron. 2021 Mar; 109(6):997–1012.e9. doi: 10.1016/j.neuron.2021.01.003.

Ecker A, Romani A, Sáray S, Káli S, Migliore M, Falck J, Lange S, Mercer A, Thomson AM, Muller E, Reimann MW, Ramaswamy S. Data-driven integration of hippocampal CA1 synaptic physiology in silico. Hippocampus. 2020; n/a(n/a). doi: 10.1002/hipo.23220, _eprint: https://onlinelibrary.wiley.com/doi/pdf/10.1002/hipo.23220.

Ferguson KA, Chatzikalymniou AP, Skinner FK. Combining Theory, Model, and Experiment to Explain How Intrinsic Theta Rhythms Are Generated in an In Vitro Whole Hippocampus Preparation without Oscillatory Inputs. eNeuro. 2017 Aug; 4(4). doi: 10.1523/ENEURO.0131-17.2017.

Ferguson KA, Huh CYL, Amilhon B, Manseau F, Williams S, Skinner FK. Network models provide insights into how oriens-lacunosum-moleculare and bistratified cell interactions influence the power of local hippocampal CA1 theta oscillations. Frontiers in Systems Neuroscience. 2015; 9:110. doi: 10.3389/fnsys.2015.00110.

Ferguson KA, Skinner FK. Hippocampal Theta, Gamma, and Theta/Gamma Network Models. In: Jaeger D, Jung R, editors. Encyclopedia of Computational Neuroscience Springer; 2015.p. 1340–1352. doi: 10.1007/978-1-4614-6675-8_27.

Fishell G, Kepecs A. Interneuron Types as Attractors and Controllers. Annual Review of Neuroscience. 2020 Jul; 43(1):1–30. doi: 10.1146/annurev-neuro-070918-050421, publisher: Annual Reviews.

Freund TF, Buzsáki G. Interneurons of the hippocampus. Hippocampus. 1996; 6(4):347–470. doi: 10.1002/(SICI)1098-1063(1996)6:4<347::AID-HIPO1>3.0.CO;2-I.

Freund TF. Interneuron Diversity series: Rhythm and mood in perisomatic inhibition. Trends in Neurosciences. 2003 Sep; 26(9):489–495. doi: 10.1016/S0166-2236(03)00227-3.

Freund TF, Katona I. Perisomatic Inhibition. Neuron. 2007 Oct; 56(1):33–42. doi: 10.1016/j.neuron.2007.09.012.

Goutagny R, Gu N, Cavanagh C, Jackson J, Chabot JG, Quirion R, Krantic S, Williams S. Alterations in hippocampal network oscillations and theta-gamma coupling arise before amyloid beta overproduction in a mouse model of Alzheimer's disease. The European Journal of Neuroscience. 2013; 37(12):1896–1902. doi: 10.1111/ejn.12233.

Gouwens NW, Sorensen SA, Baftizadeh F, Budzillo A, Lee BR, Jarsky T, Alfiler L, Baker K, Barkan E, Berry K, Bertagnolli D, Bickley K, Bomben J, Braun T, Brouner K, Casper T, Crichton K, Daigle TL, Dalley R, de Frates RA, et al. Integrated Morphoelectric and Transcriptomic Classification of Cortical GABAergic Cells. Cell. 2020 Nov; 183(4):935–953.e19. doi: 10.1016/j.cell.2020.09.057.

Guet-McCreight A, Skinner FK, Topolnik L. Common Principles in Functional Organization of VIP/Calretinin Cell-Driven Disinhibitory Circuits Across Cortical Areas. Frontiers in Neural Circuits. 2020; 14. doi: 10.3389/fncir.2020.00032, publisher: Frontiers.

Hamm V, Héraud C, Cassel JC, Mathis C, Goutagny R. Precocious Alterations of Brain Oscillatory Activity in Alzheimer's Disease: A Window of Opportunity for Early Diagnosis and Treatment. Frontiers in Cellular Neuroscience. 2015; p. 491. doi: 10.3389/fncel.2015.00491.

Harris KD, Hochgerner H, Skene NG, Magno L, Katona L, Gonzales CB, Somogyi P, Kessaris N, Linnarsson S, Hjerling-Leffler J. Classes and continua of hippocampal CA1 inhibitory neurons revealed by single-cell transcriptomics. PLOS Biology. 2018 Jun; 16(6):e2006387. doi: 10.1371/journal.pbio.2006387.

Jensen O, Colgin LL. Cross-frequency coupling between neuronal oscillations. Trends in Cognitive Sciences. 2007 Jul; 11(7):267–269. doi: 10.1016/j.tics.2007.05.003.

Karlsson AE, Lindenberger U, Sander MC. Out of Rhythm: Compromised Precision of Theta-Gamma Coupling Impairs Associative Memory in Old Age. Journal of Neuroscience. 2022 Mar; 42(9):1752–1764. doi: 10.1523/JNEUROSCI.1678-21.2021.

Kepecs A, Fishell G. Interneuron cell types are fit to function. Nature. 2014 Jan; 505(7483):318–326. doi: 10.1038/nature12983.

Kessaris N, Denaxa M. Cortical interneuron specification and diversification in the era of big data. Current Opinion in Neurobiology. 2023 Jun; 80:102703. doi: 10.1016/j.conb.2023.102703.

Kitchigina VF. Alterations of Coherent Theta and Gamma Network Oscillations as an Early Biomarker of Temporal Lobe Epilepsy and Alzheimer's Disease. Frontiers in Integrative Neuroscience. 2018; 12. doi: 10.3389/fnint.2018.00036.

Klausberger T, Somogyi P. Neuronal Diversity and Temporal Dynamics: The Unity of Hippocampal Circuit Operations. Science. 2008 Jul; 321(5885):53 –57. doi: 10.1126/science.1149381.

Kragel JE, VanHaerents S, Templer JW, Schuele S, Rosenow JM, Nilakantan AS, Bridge DJ. Hippocampal theta coordinates memory processing during visual exploration. eLife. 2020 Mar; 9:e52108. doi: 10.7554/eLife.52108, publisher: eLife Sciences Publications, Ltd.

Kramis R, Vanderwolf CH, Bland BH. Two types of hippocampal rhythmical slow activity in both the rabbit and the rat: Relations to behavior and effects of atropine, diethyl ether, urethane, and pentobarbital. Experimental Neurology. 1975 Oct; 49(1):58–85. doi: 10.1016/0014-4886(75)90195-8.

Kropff E, Carmichael JE, Moser EI, Moser MB. Frequency of theta rhythm is controlled by acceleration, but not speed, in running rats. Neuron. 2021 Mar; 109(6):1029–1039.e8. doi: 10.1016/j.neuron.2021.01.017.

Leão RN, Mikulovic S, Leão KE, Munguba H, Gezelius H, Enjin A, Patra K, Eriksson A, Loew LM, Tort ABL, Kullander K. OLM interneurons differentially modulate CA3 and entorhinal inputs to hippocampal CA1 neurons. Nature Neuroscience. 2012; 15(11):1524–1530. doi: 10.1038/nn.3235.

Lisman J. The theta/gamma discrete phase code occuring during the hippocampal phase precession may be a more general brain coding scheme. Hippocampus. 2005; 15(7):913–922. doi: 10.1002/hipo.20121.

McBain CJ, Fisahn A. Interneurons unbound. Nature Reviews Neuroscience. 2001; 2(1):11–23. doi: 10.1038/35049047.

Musaeus CS, Nielsen MS, Musaeus JS, Høgh P. Electroencephalographic Cross-Frequency Coupling as a Sign of Disease Progression in Patients With Mild Cognitive Impairment: A Pilot Study. Frontiers in Neuroscience. 2020 Aug; 14:790. doi: 10.3389/fnins.2020.00790.

Müller C, Remy S. Dendritic inhibition mediated by O-LM and bistratified interneurons in the hippocampus. Frontiers in Synaptic Neuroscience. 2014; 6:23. doi: 10.3389/fnsyn.2014.00023.

Navas-Olive A, Valero M, Jurado-Parras T, Salas-Quiroga Ad, Averkin RG, Gambino G, Cid E, Prida LMdl. Multimodal determinants of phase-locked dynamics across deep-superficial hippocampal sublayers during theta oscillations. Nature Communications. 2020; 11(1):1–14. doi: 10.1038/s41467-020-15840-6, number: 1.

Pedregosa F, Varoquaux G, Gramfort A, Michel V, Thirion B, Grisel O, Blondel M, Prettenhofer P, Weiss R, Dubourg V, Vanderplas J, Passos A, Cournapeau D, Brucher M, Perrot M, Duchesnay E. Scikit-learn: Machine Learning in Python. Journal of Machine Learning Research. 2011; 12:2825–2830.

Pelkey KA, Chittajallu R, Craig MT, Tricoire L, Wester JC, McBain CJ. Hippocampal GABAergic Inhibitory Interneurons. Physiological Reviews. 2017 Oct; 97(4):1619–1747. doi: 10.1152/physrev.00007.2017.

Ponzi A, Dura-Bernal S, Migliore M. Theta-gamma phase amplitude coupling in a hippocampal CA1 microcircuit. PLOS Computational Biology. 2023 Mar; 19(3):e1010942. doi: 10.1371/journal.pcbi.1010942, publisher: Public Library of Science.

Ratliff JM, Batista-Brito R. The Interneuron Class Struggle. Cell. 2020 Nov; 183(4):845–847. doi: 10.1016/j.cell.2020.10.034.

Scheffer-Teixeira R, Belchior H, Caixeta FV, Souza BC, Ribeiro S, Tort ABL. Theta Phase Modulates Multiple Layer-Specific Oscillations in the CA1 Region. Cerebral Cortex. 2012 Jan; 22(10):2404–2414. doi: 10.1093/cercor/bhr319.

Scheffer-Teixeira R, Tort ABL. Theta-Gamma Cross-Frequency Analyses (Hippocampus). In: Jaeger D, Jung R, editors. Encyclopedia of Computational Neuroscience New York, NY: Springer New York; 2022.p. 3419–3433. https://doi.org/10.1007/978-1-0716-1006-0_100658, doi: 10.1007/978-1-0716-1006-0_100658.

Skinner FK, Rich S, Lunyov AR, Lefebvre J, Chatzikalymniou AP. A Hypothesis for Theta Rhythm Frequency Control in CA1 Microcircuits. Frontiers in Neural Circuits. 2021; 15. doi: 10.3389/fncir.2021.643360, publisher: Frontiers.

Soltesz I, Losonczy A. CA1 pyramidal cell diversity enabling parallel information processing in the hippocampus. Nature Neuroscience. 2018 Apr; 21(4):484–493. doi: 10.1038/s41593-018-0118-0.

Strange BA, Witter MP, Lein ES, Moser EI. Functional organization of the hippocampal longitudinal axis. Nature Reviews Neuroscience. 2014 Oct; 15(10):655–669. doi: 10.1038/nrn3785.

Tendler A, Wagner S. Different types of theta rhythmicity are induced by social and fearful stimuli in a network associated with social memory. eLife. 2015 Feb; 4:e03614. doi: 10.7554/eLife.03614.

Tiesinga P, Sejnowski TJ. Cortical enlightenment: are attentional gamma oscillations driven by ING or PING? Neuron. 2009 Sep; 63(6):727–732. doi: 10.1016/j.neuron.2009.09.009.

Traub RD, Miles R, Buzsáki G. Computer simulation of carbachol-driven rhythmic population oscillations in the CA3 region of the in vitro rat hippocampus. The Journal of physiology. 1992; 451:653–672.

Tyan L, Chamberland S, Magnin E, Camiré O, Francavilla R, David LS, Deisseroth K, Topolnik L. Dendritic Inhibition Provided by Interneuron-Specific Cells Controls the Firing Rate and Timing of the Hippocampal Feedback Inhibitory Circuitry. The Journal of Neuroscience. 2014 Mar; 34(13):4534–4547. doi: 10.1523/JNEUROSCI.3813-13.2014.

Wheeler DW, White CM, Rees CL, Komendantov AO, Hamilton DJ, Ascoli GA. Hippocampome.org: a knowledge base of neuron types in the rodent hippocampus. eLife. 2015 Nov; 4:e09960. doi: 10.7554/eLife.09960.

Whittington MA, Traub RD, Kopell N, Ermentrout B, Buhl EH. Inhibition-based rhythms: experimental and mathematical observations on network dynamics. International Journal of Psychophysiology: Official Journal of the International Organization of Psychophysiology. 2000; 38(3):315–336. doi: 10.1016/s0167-8760(00)00173-2.

Wilson HR, Cowan JD. Excitatory and Inhibitory Interactions in Localized Populations of Model Neurons. Biophysical Journal. 1972 Jan; 12(1):1–24. doi: 10.1016/S0006-3495(72)86068-5.

Wilson MA, Varela C, Remondes M. Phase organization of network computations. Current Opinion in Neurobiology. 2015 Apr; 31:250–253. doi: 10.1016/j.conb.2014.12.011.

Yao Z, Velthoven CTJv, Nguyen TN, Goldy J, Sedeno-Cortes AE, Baftizadeh F, Bertagnolli D, Casper T, Chiang M, Crichton K, Ding SL, Fong O, Garren E, Glandon A, Gouwens NW, Gray J, Graybuck LT, Hawrylycz MJ, Hirschstein D, Kroll M, et al. A taxonomy of transcriptomic cell types across the isocortex and hippocampal formation. Cell. 2021 Jun; 184(12):3222–3241.e26. doi: 10.1016/j.cell.2021.04.021, publisher: Elsevier.

Zhang X, Zhong W, Brankačk J, Weyer SW, Müller UC, Tort ABL, Draguhn A. Impaired theta-gamma coupling in APP-deficient mice. Scientific Reports. 2016 Feb; 6:21948. doi: 10.1038/srep21948.

Appendix 0—table 2. Synaptic weight values and characteristics for the ten selected parameter sets

Set	$w_{PYR \to PYR/BiC/PV}$ *(au)*	$w_{BiC \to PYR}$ *(au)*	$w_{CCK \to CCK/PV}$ *(au)*	$w_{PV \to PV/PYR/CCK}$ *(au)*	*PV/BiC ratio*	*max CCK (Hz)*	*Theta freq (Hz)*
0	0.05/0.04/0.02	-0.02	-0.15/-0.15	-0.055/-0.03/-0.075	0.71	10.11	7.75
1	0.05/0.04/0.02	-0.02	-0.15/-0.107	-0.055/-0.03/-0.075	0.71	6.29	6.5
2	0.05/0.04/0.02	-0.019	-0.15/-0.15	-0.055/-0.03/-0.075	0.71	8.08	8.0
3	0.05/0.04/0.036	-0.02	-0.15/-0.107	-0.055/-0.03/-0.075	1.05	7.38	4.5
4	0.05/0.04/0.02	-0.019	-0.15/-0.078	-0.055/-0.03/-0.075	0.72	5.71	6.75
5	0.05/0.04/0.02	-0.02	-0.15/-0.11	-0.055/-0.035/-0.075	0.83	8.18	6.5
6	0.05/0.04/0.02	-0.02	-0.15/-0.024	-0.055/-0.025/-0.075	0.71	4.76	8.5
7	0.05/0.04/0.02	-0.02	-0.48/-0.078	-0.055/-0.03/-0.075	0.73	5.45	6.75
8	0.05/0.04/0.027	-0.019	-0.27/-0.078	-0.055/-0.03/-0.052	0.85	9.92	7.0
9	0.05/0.04/0.02	-0.019	-1.03/-0.086	-0.055/-0.03/-0.071	0.72	5.46	6.75

All of the synaptic weight values for the ten parameter sets are given. Other parameter values are given in TABLE 1. Unless otherwise indicated, STIM is set to zero for all cell types. Also shown are the activity ratios of PV/BiC and the maximal CCK activities which formed part of the constraints (see details in Model and methods section), as well as the theta frequency.

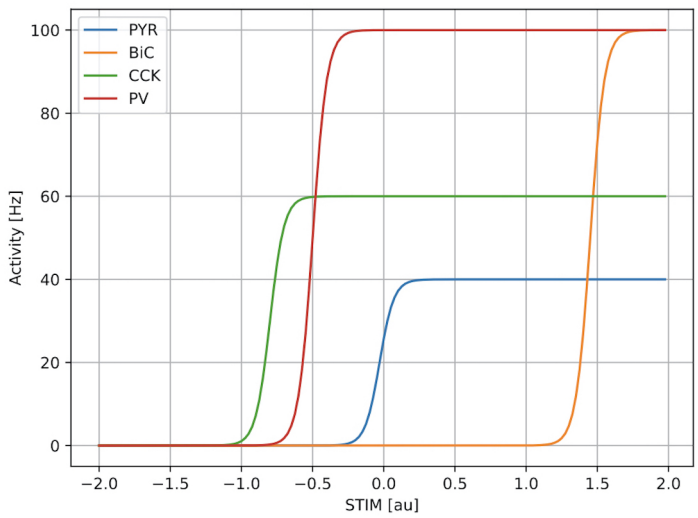

Figure 2—figure supplement 1. Intrinsic firing rates for the four cell types in the PRM. As STIM is varied, the firing of the four cell types changes as shown.

Appendix 0—table 3. Theta and gamma power changes with connection removals

Set	*Connection type removal*	*Theta power ratio*[1]	*Gamma power ratio*[1]	*Sufficient?*[2] *(Y/N)*
0-3,5	PYR→PYR*	≈ 0	> 0.2	N
4	PYR→PYR*	≈ 0	0.06	N
6-9	PYR→PYR*	≈ 0	< 0.05 ($\neq 0$)	N
0-9	PYR→BiC	≈ 0	≈ 0	N
0,2	PYR→PV	≈ 0	≈ 0	N
1,3	PYR→PV	> 0.2	> 0.2	N
4-9	PYR→PV	> 0.2	> 0.2	**Y**
0-9	BiC→PYR*	≈ 0	≈ 0	N
0-9	PV→PYR*	≈ 0	≈ 0	N
0-9	PV→PV	≈ 0	≈ 0	N
0,2,3,5	PV→CCK	< 0.07 ($\neq 0$)	> 0.2	N
1	PV→CCK	0.11	> 0.2	N
4	PV→CCK	0.17	> 0.2	N
6,9	PV→CCK	> 0.2	> 0.2	**Y**
7	PV→CCK	> 0.2	> 0.2	N
8	PV→CCK	0.12	> 0.2	N
0-9	CCK→PV*	≈ 0	< 0.01 ($\neq 0$)	N
0-5,7-9	CCK→CCK	≈ 0	≈ 0	N
6	CCK→CCK	> 0.2	> 0.2	**Y**

[1]*Theta or gamma power ratio is the ratio of the theta power when the particular connection is removed divided by the reference theta or gamma power when no connections are removed.*
[2]*Sufficient means that both theta and gamma powers are large enough to be considered to have theta-gamma coupled rhythms to be present. $> 25\%$ of the reference power was used as the threshold. Note that if $> 20\%$ was used, more cases would have been considered to be sufficient.*
**Due to applied constraints (see FIGURE 2C-F), removal of these connections is expected to yield no theta rhythms, and hence no theta-gamma coupled rhythms.*
See Model and methods section for further details.

Appendix 0—table 4. Changes in amplitude and interspike intervals of LFP theta with and without CCK

Set	*Amplitude (au)*		*Mean ISI (s)*		*Std ISI (s)*	
	CCK present	*CCK absent*	*CCK present*	*CCK absent*	*CCK present*	*CCK absent*
0	38.2	38.1	0.128	0.147	0.011	0.025
1	38.5	37.9	0.153	0.135	0.0	0.028
2	38.2	38.1	0.126	0.146	0.006	0.028
4	38.4	38.4	0.146	0.167	0.006	0.0
6	38.3	38.3	0.117	0.117	0.0	0.0
7	38.2	37.9	0.147	0.140	0.002	0.025
9	38.4	38.3	0.147	0.167	0.0	0.032

ISI = interspike interval between theta events; Std = standard deviation.

Appendix 0—table 5. Statistical comparisons between cell types for theta and gamma power and ranges

	Theta power			***Gamma power***			**STIM range**	
Cell 1	*Cell 2*	*p-value*	*Cell 1*	*Cell 2*	*p-value*	*Cell 1*	*Cell 2*	*p-value*
PYR	BiC	6.3×10^{-2} *	PYR	BiC	1.9×10^{-2}	CCK	PYR	1.1×10^{-5}
PYR	CCK	1.1×10^{-5}	PYR	CCK	1.5×10^{-3}	CCK	BiC	2.2×10^{-5}
PYR	PV	1.1×10^{-5}	PYR	PV	4.9×10^{-4}	CCK	PV	2.2×10^{-5}
BiC	PV	1.1×10^{-5}	PV	BiC	1.9×10^{-1} *			
BiC	CCK	1.1×10^{-5}	PV	CCK	1.9×10^{-2}			

** Not statistically significant. These comparisons are related to FIGURE 5**A,B,D**. Comparisons were done using Mann-Whitney (95%, p<0.05).*

Appendix 0—table 6. Statistical comparisons between cell types for theta frequency

	Theta frequency	
Cell 1	*Cell 2*	*p-value*
PYR	BiC	3.3×10^{-4} *
PYR	CCK	2.1×10^{-3}
PYR	PV	1.1×10^{-5}
BiC	CCK	7.5×10^{-2} *
BiC	PV	3.9×10^{-3}
CCK	PV	1.1×10^{-5}

** Not statistically significant. These comparisons are related to FIGURE 5**C**.*
Comparisons were done using Mann-Whitney (95%, p<0.05).

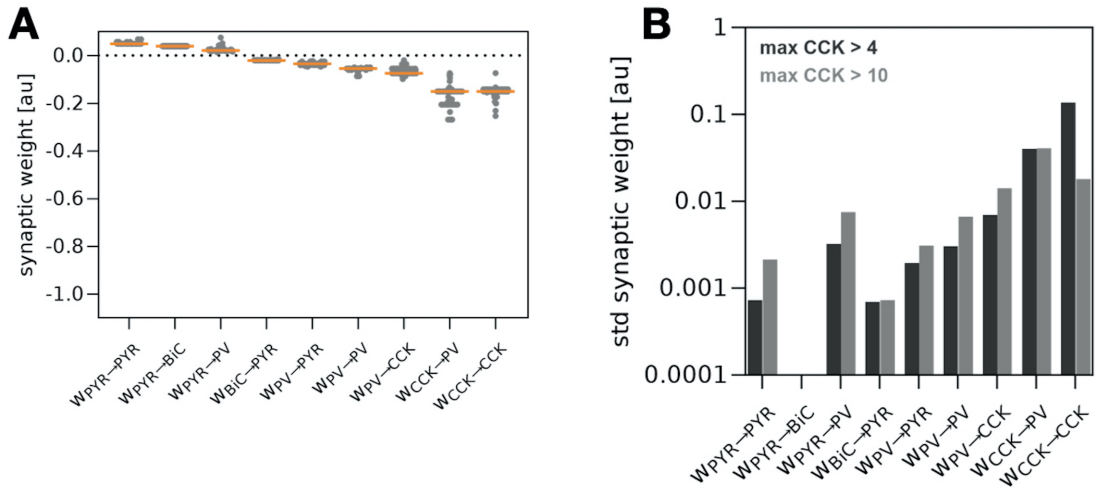

Figure 3—figure supplement 1. Additional distributions.
A. Distribution of synaptic weights for each of the nine different connections in the PRM, from 200 constrained parameter sets of synaptic weights found when running the genetic algorithm for a maximal firing of CCK constrained to be greater than 10 (compare with FIGURE 3*A* when maximal firing of CCK is 4). The orange line depicts the median. **B.** Bar graph showing the standard deviations (std) of the synaptic weights for each of the nine different connections when maximal firing of CCK was either 4 or 10 as labelled.

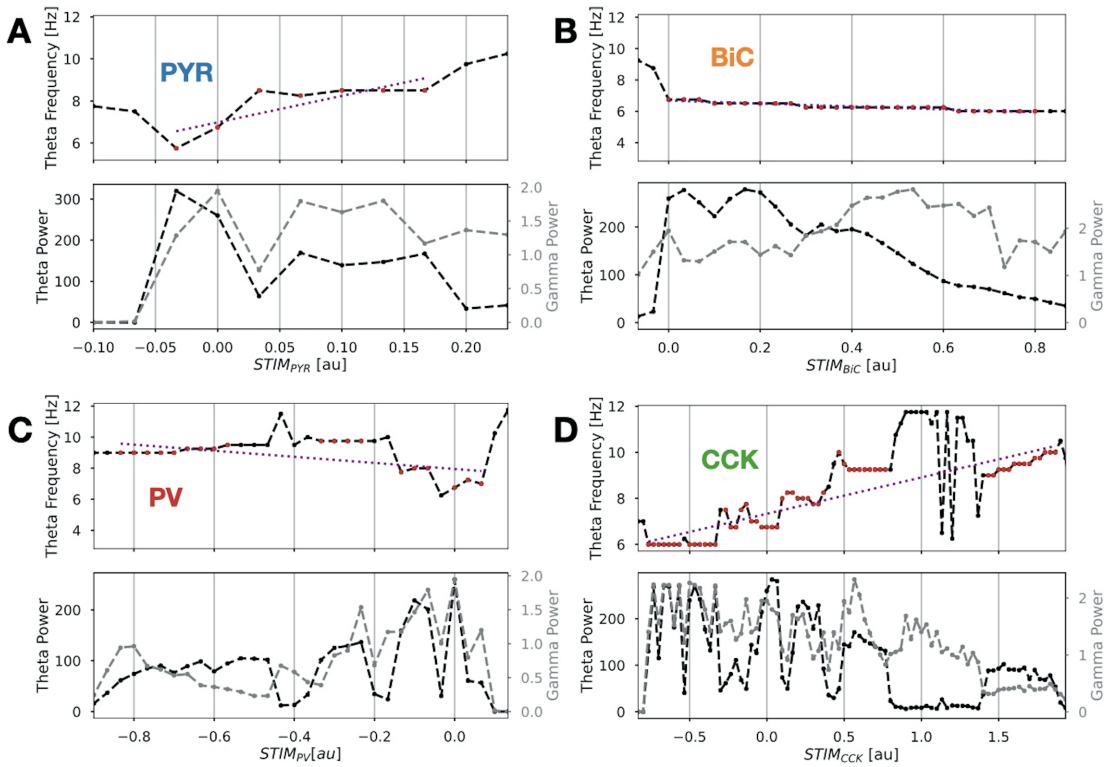

Figure 5—figure supplement 1. Example illustration of slope quantification for theta and gamma powers and theta frequency with STIM variation.

LFP theta frequency (top parts) and theta and gamma power (bottom parts) in the four-cell system with varying STIM to PYR **(A)**, BiC **(B)**, PV **(C)**, and CCK **(D)** cell types are plotted using *Set 4* parameter values. The plots are truncated to be centred around the values of STIM that allow the system to exhibit theta-gamma coupled rhythms, and one can immediately see that there is a wider range (i.e., difference between the maximum and minimum) of STIM values for CCK relative to the other cell types. This is summarized in FIGURE 5*D*. The STIM values where sufficient theta-gamma coupled rhythms occur are marked using red dots on the theta frequency plots. The dashed purple line shows the line best fitting the variation of theta frequency with STIM using only the points (red dots) where theta-gamma oscillations occur. Similar lines (not shown) and fits were done for theta and gamma powers. The slopes of the theta and gamma power line fits are used to make the plots shown in FIGURE 5*A, B*, and in *C*, the plot using the slopes of the theta frequency line fits is shown. We note that changes in theta and gamma powers and theta frequency do not necessarily change in a smooth fashion. This jaggedness is due to the dynamic, nonlinear coupling interactions occurring between theta and gamma rhythms which affects the amplitude and expression of the theta-gamma coupled rhythms as STIM is varied, and hence theta and gamma powers and theta frequency. We illustrate this in *Supplementary Figure*2.

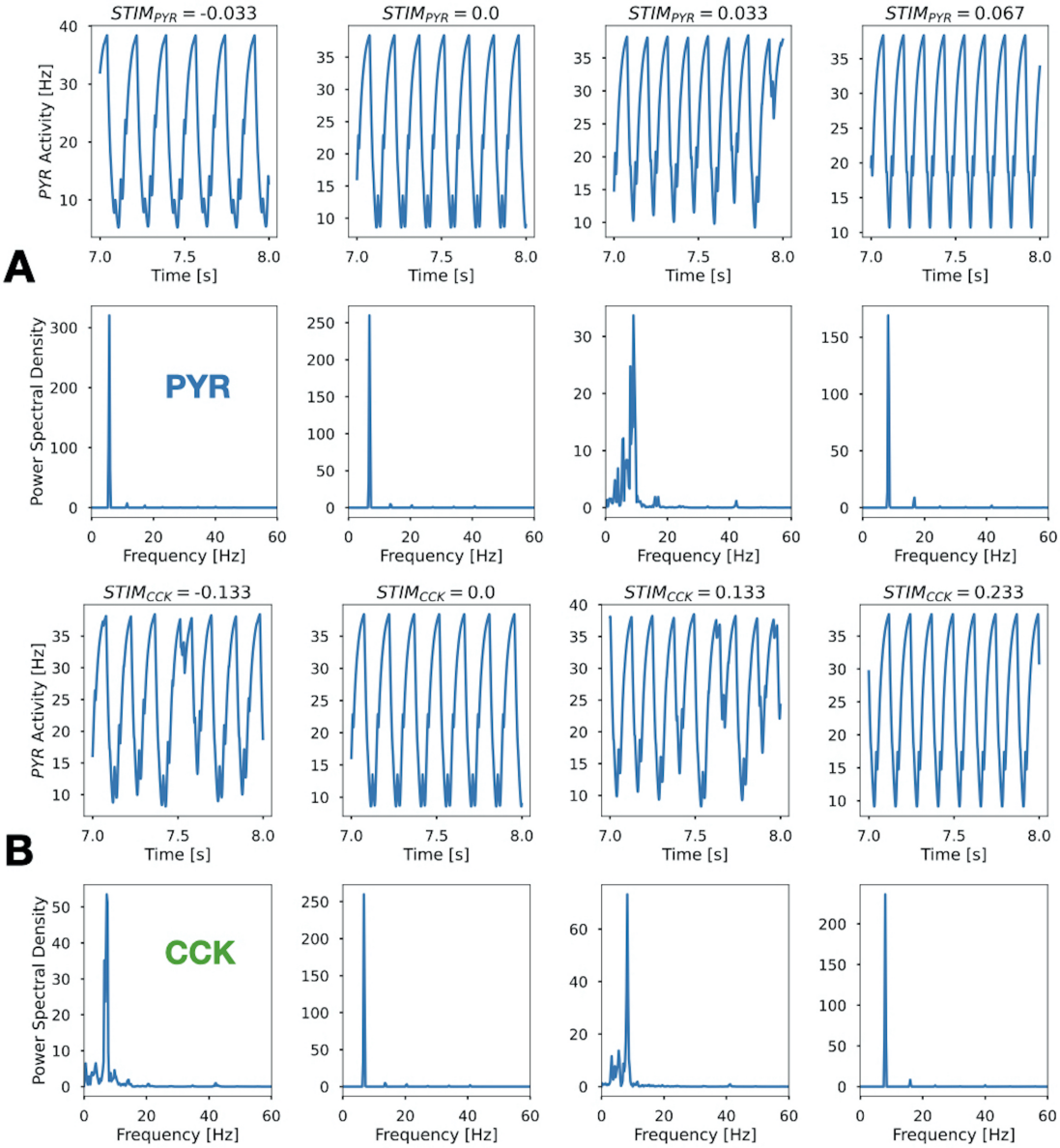

Figure 5—figure supplement 2. Example illustration of PYR activities and their power spectral densities.

PYR activity outputs for four different STIM values and the power spectral density (PSD) associated with the PYR activity (LFP representation). **A.** STIM values when applied to PYR **B.** STIM values when applied to CCK. This is for *Set 4* parameter values, representing specific red dots shown in *Supplementary Figure*1. From these selected examples, it is clear why there is jaggedness in the theta and gamma powers and theta frequency. In viewing the PSDs, it is clear that the theta powers are much larger than the gamma powers. PSD units are Hz.

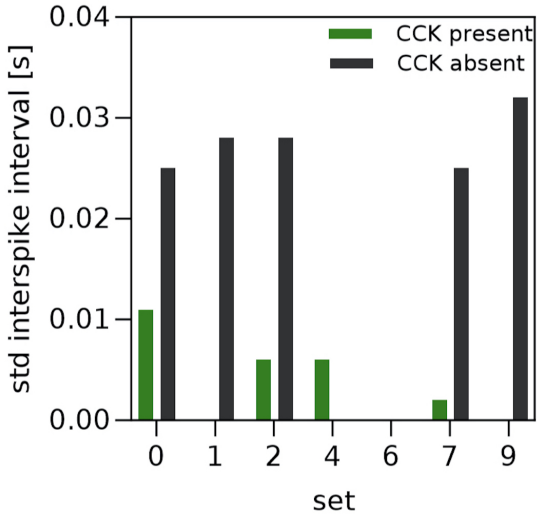

Figure 6—figure supplement 1. Changes in regularity of theta events.
Bar graph showing how the theta rhythm regularity is affected by the presence of absence of CCK during ongoing theta-gamma coupled rhythms for seven of the ten sets as labelled. If no bar is present, then the standard deviation (std) is zero. The specific values are given in TABLE 4.

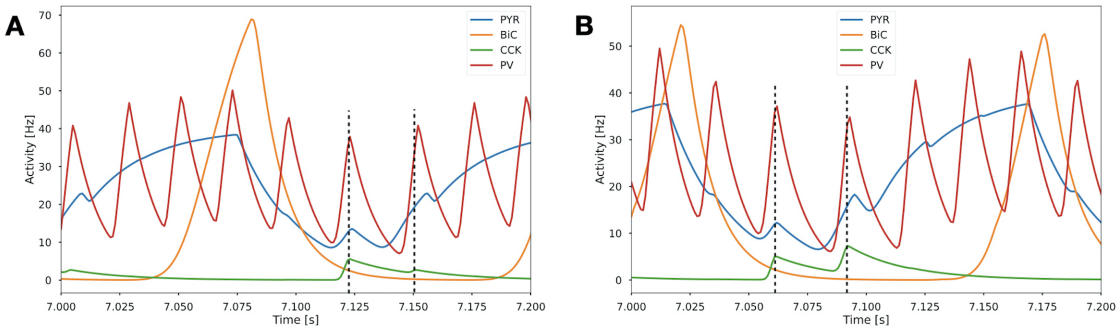

Figure 7—figure supplement 1. A blow up of activities to illustrate timings.
Activities of the four cell types are shown for a 0.1 second range for *Set 4* parameter values **(A)**, and *Set 5* parameter values **(B)**. The two-phase process schematized in FIGURE 7C where CCK initiates the gamma in the first phase is illustrated by the vertical lines at the peaks of CCK preceding both PV and PYR.